Geomorphology

Weathering processes and rates of scarp retreat in a Mediterranean mountain environment: a multi-analytical approach from terrestrial laser scanning to microscale surveys

--Manuscript Draft--

Manuscript Number:	GEOMOR-11450R2
Article Type:	Research Paper
Keywords:	granite landforms; weathering patterns; multitemporal analysis; geomorphic dynamics
Corresponding Author:	Fabio Scarciglia, PhD University of Calabria: Universita della Calabria Arcavacata di Rende (CS), ITALY
First Author:	Fabio Scarciglia, PhD
Order of Authors:	Fabio Scarciglia, PhD
	Antonella Marsico
	Domenico Capolongo
Abstract:	Estimating the rates of Earth surface processes may provide a deeper comprehension of landscape shaping at different spatial/temporal scales in the light of ongoing or future climate changes and geomorphological hazards. This study explores the use of terrestrial laser scanner combined with macro/micromorphological and compositional analyses to assess three-year surface and volume changes on three granodiorite scarps in a Mediterranean upland environment (Sila Massif, Italy), estimate erosion/accumulation rates and relate them to specific geomorphic processes, weathering patterns and grades. The three scarps, affected by intermediate to high weathering grade classes, respond differently according to aspect and grain size. On coarser-grained granite of the W-facing, scarp 1 rounded weathering patterns developed because of the moister, less insolated conditions. On the finer-grained rocks of the SE-facing scarp 2, with prolonged insolation and temporary moisture, angular patterns prevail. Fine vs. coarse weathered material detached from the scarps is facilitated by prevalent chemical or physical rock degradation processes. On scarp 3, the coexistence of zones affected by pronounced physical breakdown and others influenced by pervasive chemical weathering is due to intermediate microclimatic conditions brought about by varying E and NE-facing aspect of the scarp. Rock jointing likely controls rockfall processes. The average retreat/advance rates of the scarps range from n x 10 -6 to 10 -2 m yr –1 , with net erosion rates in the range 1 x 10 -2 – 3 x 10 -4 m yr –1 and are consistent with literature data. 3D models also allow the assessment of pre-failure landslide processes affecting the scarps and their relationships with weathering.

Weathering processes and rates of scarp retreat in a Mediterranean mountain environment: a multi-analytical approach from terrestrial laser scanning to microscale surveys

Fabio Scarciglia[1,*], **Antonella Marsico**[2], **Domenico Capolongo**[2]

[1] *Dipartimento di Biologia, Ecologia e Scienze della Terra (DiBEST), Università della Calabria, Via P. Bucci – Cubo 15B, 87036 Arcavacata di Rende (CS), Italy*

[2] *Dipartimento di Scienze della Terra e Geoambientali, Università degli Studi di Bari "Aldo Moro", Via E. Orabona 4, 70125 Bari, Italy*

[*] Corresponding author

E-mail address: fabio.scarciglia@unical.it (F. Scarciglia)

Abstract

Estimating the rates of Earth surface processes may provide a deeper comprehension of landscape shaping at different spatial/temporal scales in the light of ongoing or future climate changes and geomorphological hazards. This study explores the use of terrestrial laser scanner combined with macro/micromorphological and compositional analyses to assess three-year surface and volume changes on three granodiorite scarps in a Mediterranean upland environment (Sila Massif, Italy), estimate erosion/accumulation rates and relate them to specific geomorphic processes, weathering patterns and grades. The three scarps, affected by intermediate to high weathering grade classes, respond differently according to aspect and grain size. On coarser-grained granite of the W-facing, scarp 1 rounded weathering patterns developed because of the moister, less insolated conditions. On the finer-grained rocks of the SE-facing scarp 2, with

prolonged insolation and temporary moisture, angular patterns prevail. Fine vs. coarse weathered material detached from the scarps is facilitated by prevalent chemical or physical rock degradation processes. On scarp 3, the coexistence of zones affected by pronounced physical breakdown and others influenced by pervasive chemical weathering is due to intermediate microclimatic conditions brought about by varying E and NE-facing aspect of the scarp. Rock jointing likely controls rockfall processes. The average retreat/advance rates of the scarps range from n x 10^{-6} to 10^{-2} m yr^{-1}, with net erosion rates in the range 1 x 10^{-2} – 3 x 10^{-4} m yr^{-1} and are consistent with literature data. 3D models also allow the assessment of pre-failure landslide processes affecting the scarps and their relationships with weathering.

Keywords: granite landforms, weathering patterns, multitemporal analysis, climate, geomorphic dynamics

1. Introduction

Over recent decades there has been a growing interest in estimating the rates of Earth surface processes (e.g., weathering, soil development, denudation/erosion) which shape the landscape at different spatial and temporal scales. Approaches have spanned from (a) regional, (b) landscape or watershed, (b) hillslope, landform and site/microsite to (c) laboratory scales, and from long-term (millions of years to millennia and centuries) to short-term (decades to years and even shorter) time lapses (Oguchi, 2013; Viles, 2013).

A number of approaches and techniques have been used so far, such as (1) uranium-series isotopes, elemental and mineralogical analyses and mass balance methods for estimating weathering rates (Dosseto et al., 2008; Dosseto et al., 2019; Sun et al., 2019); (2) soil chronosequences, geochemical indices and ratios, chronofunctions or mechanistic models to

estimate rates of soil development and/or specific pedogenic processes (Calero et al., 2008; Cornu et al., 2009; Lair et al., 2009; Vanwalleghem et al., 2013; Roquero et al., 2015; Scarciglia et al., 2015); (3) missing volume calculations (Amato et al., 2003; Schiattarella et al., 2006; Pérez-Peña et al., 2009; Scarciglia, 2015); (4) comparison of multitemporal historical maps/aerial photos (Aucelli et al., 2016; Conforti and Buttafuoco, 2017), terrestrial cosmogenic nuclides (such as ^{10}Be, ^{26}Al, ^{36}Cl) and anthropogenic fallout isotopes derived from nuclear weapon tests and accidents (^{137}Cs, $^{239+240}$Pu) to quantify soil production (Heimsath et al., 1997; Granger and Riebe, 2014), (5) long-term denudation (Heimsath et al., 2001; Heimsath et al., 2012; Willenbring and von Blanckenburg, 2010; Raab et al., 2021) and short-term erosion rates (Alewell et al., 2014; Meusburger et al., 2016).

Different methods have been adopted to estimate retreat rates of rock scarps under different climate conditions, time intervals and lithologies, based on indirect approaches such as the calculation of talus slope volume fed by rockfall processes (Hinchliffe and Ballantyne, 1999; Curry and Morris, 2004), radiocarbon dating of the charcoal remains found in debris slopes of stepped flatirons (Gutiérrez Elorza and Sesé Martínez, 2001), or direct techniques such as cosmogenic nuclides (Domènech et al., 2018) and terrestrial laser scanner (TLS) (Day et al., 2013a).

Among several published papers which have used laser scanner as a tool for the geosciences, there has been a special focus on the assessment of natural hazards (Telling et al., 2017), including the coupling of ancillary techniques for the spatial zonation of rockfalls (Fanos and Pradhan, 2019), their prediction through the detection of precursory deformation (Abellán et al., 2010) and the modeling of potential runout trajectories (Salvini et al., 2013). Other papers have focused on reconstructing the evolution of the cliff-talus system (Bonneau and Hutchinson, 2019), the evaluation of topographic pattern changes and the quantification of watershed-scale sediment budget in different environments (Day et al., 2013a; Day et al., 2013b; Vericat et al., 2014), as well as testing the role of different slope aspects in controlling types and speeds of morphodynamic processes (Nadal Romero et al., 2015).

Although weathering controls mass fluxes and landform evolution and is considered a predisposing factor of varying morphodynamic processes including erosion, sedimentation and landslides (Chigira and Yokoyama, 2005; Borrelli et al., 2007; Scarciglia et al., 2007; Hinderer, 2012; Pope, 2013; Viles, 2013; Borrelli et al., 2018), the relationships between weathering features and rockwall retreat rates at the weathering profile scale have rarely been explored. Most of the papers focused on sea cliff retreat rates measured with TLS or LiDAR and their relationship with slope instability (Katz and Mushkin, 2013; Kuhn and Prüfer, 2014; Caputo et al., 2018), whereas quantitative estimations from inland mountain sites have been rarer (Fischer et al., 2011; Hartmeyer et al., 2020).

The Sila Massif upland plateau is a promising pilot area in the central Mediterranean, which is well-suited to compare present-day scarp retreat rates, estimated in this study by using TLS techniques, with long- to short-term surface erosion rates. There is already a deep understanding of current and past landscapes and their evolution (Le Pera and Sorriso-Valvo, 2000; Molin et al., 2004, 2012), sediment generation (Le Pera et al., 2001; von Eynatten et al., 2016), weathering (Biondino et al., 2020; Perri, 2020), soil formation processes, geomorphic dynamics and anthropogenic impact (Scarciglia et al., 2007, 2016; Pelle et al., 2013) in this area. In addition, some data are already available on Quaternary erosion rates due to fluvial transport (Olivetti et al., 2012; Cyr et al., 2014) and surface lowering/denudation obtained usingcosmogenic ^{10}Be (Scarciglia, 2015; Raab et al., 2019), and modern erosion rates and redistribution processes derived from fallout $^{239+240}Pu$ (Raab et al., 2018), $^{210}Pb_{ex}$ and ^{137}Cs isotopes (Scarciglia et al., 2020). This work aims to assess, for the first time, surface and volume changes due to cliff evolution by using TLS, estimating erosion/accumulation rates on three granodiorite rock scarps and relating these to weathering features, patterns and grades, assessed at both macro/microscales and using compositional data, along with specific geomorphic processes. The role of climatic parameters is also explored. This combined approach aims at achieving a deeper comprehension of the key processes and factors affecting short-term scarp evolution and slope stability, such as gravity-driven versus water erosion, physical and chemical weathering, rock

texture and composition, slope aspect control and climate, as well as their mutual relationships in a typical Mediterranean upland environment.

2. Geological, geomorphological and climatic setting

The study area is located in the Sila Massif upland (Calabria, southern Italy) (Fig. 1), the bulk structure of which consists of Paleozoic crystalline basement rocks (of medium- to high-grade metamorphism) relating to the Hercynian Peloritan-Calabrian Arc orogeny (Bonardi et al., 2001; Cirrincione et al., 2015), intruded by late Variscan granitoids ("Sila Unit"). They represent sectors of the continental crust which forms the Sila batholith (Messina et al., 1991, 2004; Liotta et al., 2008; Festa et al., 2010), locally covered by Mesozoic to Cenozoic sedimentary terranes (Van Dijk et al., 2000; Critelli et al., 2011). An uplifted low-relief landscape dominates the summit of the Sila plateau, where flat to gently-rolling planation surfaces (paleosurfaces) were shaped during the Pliocene and Pleistocene and displaced at different elevations (1000-1700 m a.s.l.) in a chessboard-like pattern by tectonic uplift (Sorriso-Valvo, 1993; Molin et al., 2012; Scarciglia, 2015). Slower uplift rates during the late Tertiary were followed by a marked acceleration during the middle Pleistocene, with repeated uplift episodes alternating with relative geomorphological stability (Westaway, 1993; Olivetti et al., 2012), prone to deep weathering processes. N–S, E–W and NW–SE trending faults and lineaments, some of which are considered seismogenetic and responsible for past historical catastrophic earthquakes (Galli et al., 2007), control the spatial distribution and evolution of the upland landforms and the drainage network (Molin et al., 2004, 2012; Spina et al., 2007; Scarciglia et al., 2016). Very slight (meters to decameters) stream dissection affects the summit landscape, with smooth wide valleys that become more deeply incised in their middle and lower reaches. Steep slopes with convex upper segments border the paleosurface limbs, creating a high relief (up to hundreds of meters in height) along the massif flanks (Martino et al., 2009; Schiattarella et al., 2013), where triangular facets occur in places. Scree taluses and detrital cones outcrop along footslopes in response to scarp retreat (Scarciglia et al., 2007). The paleosurfaces are carved across the crystalline basement and, in particular, the

130 granitoid rocks, which are mostly tonalite, monzogranite and granodiorite. There, tors and boulder
131 fields widely outcrop as a result of deep spheroidal weathering followed by long-term erosion (Le
132 Pera and Sorriso-Valvo, 2000; Scarciglia, 2015; Raab et al., 2018, 2019). Some morphotectonic
133 depressions host artificially dammed lakes, some of which were Pleistocene paleolakes.

134 The climate of the study area is warm temperate with relatively humid summers, classified as type
135 Cfb according to the Köppen classification and updates (Kottek et al., 2006), and typical of upland
136 Mediterranean zones. Mean annual precipitation is around 1240 mm, with a mean monthly
137 maximum of 180 mm recorded in November and a mean monthly minimum of 33 mm in July. Snow
138 cover usually occurs from December to April. Mean annual temperature is 8 °C, with a mean
139 monthly minimum of about −1 °C in January/February and a mean monthly maximum of 16 °C in
140 July/August (Camigliatello – Monte Curcio weather station, 1730 m a.s.l.; Centro Funzionale
141 Multirischi – ARPACAL, Calabria Region, Italy, www.cfd.calabria.it).

142

143 **3. Materials and methods**

144 *3.1 Site selection*

145 Three subvertical granodiorite rock scarps ranging from about 5 to 7 m in height (Figs. 1, 2) were
146 selected in the Sila Massif upland (southern Italy) for field surveys, sampling and laboratory
147 analyses that focused on the assessment of three-year retreat/accumulation rates, weathering
148 grade classes and patterns, and dominant geomorphic processes, as well as their mutual interplay.
149 The choice was based on previous knowledge of the main landform weathering features and
150 processes, which, for the three scarps, appear partially different (visually) in the field, especially in
151 terms of the rounded/angular patterns and coarse/fine grain size of the bedrock and of the
152 corresponding weathered material/detritus. The three scarps are road cuts and are, thus, artificial.
153 Nonetheless, they were chosen because they were easily accessible for the TLS devices and quite
154 similar (in terms of height and weathering profile features) to other natural rock scarps that occur
155 widely on the Sila plateau, such as along some stream incisions, lake borders, margins of

fluvial/lacustrine terraces or planation surfaces, major faults, hill ridges and hilltops. ~~Moreover,~~ ~~m~~Much higher scarps in the study area (from tens to hundreds of meters in height) often exhibit similar weathering and gravity-driven processes (when not densely vegetated), which cause their retreat. Moreover, several papers clearly show that both natural rock scarps and anthropogenic cuts in the Sila Massif display similar juxtapositions of weathering grade classes, varying grussification processes, debris production, rockfalls, shallow topsoils, etc. (Scarciglia et al., 2007, 2016; Borrelli et al., 2014, 2015, 2016; Perri et al., 2015). The top of scarp 1 (centered at ca. 39°17'34.24" N, 16°31'36.05" E) is located at 1488 m a.s.l., just below a hillslope that inclines from about 10° to 22°, is more than 200 m long and is covered by a dense forest dominated by pine, with occasional beech trees. The maximum height of scarp 1 is 6.5 m. Scarp 2 (39°18'33.80" N, 16°32'18.10" E, 1437 m a.s.l., max height of 6.8 m) and scarp 3 (39°19'2.63" N, 16°32'30.72" E, 1395 m a.s.l., max height of 4.6 m) are characterized by flat to gently-inclined border surfaces (≤10°), covered by grassland and shrubs, with rare to occasional isolated trees. In addition, although at a similar altitude, the three scarps have different slope aspects: scarp 1 is WNW to WSW-facing, scarp 2 is SE-facing and scarp 3 is E and NE-facing.

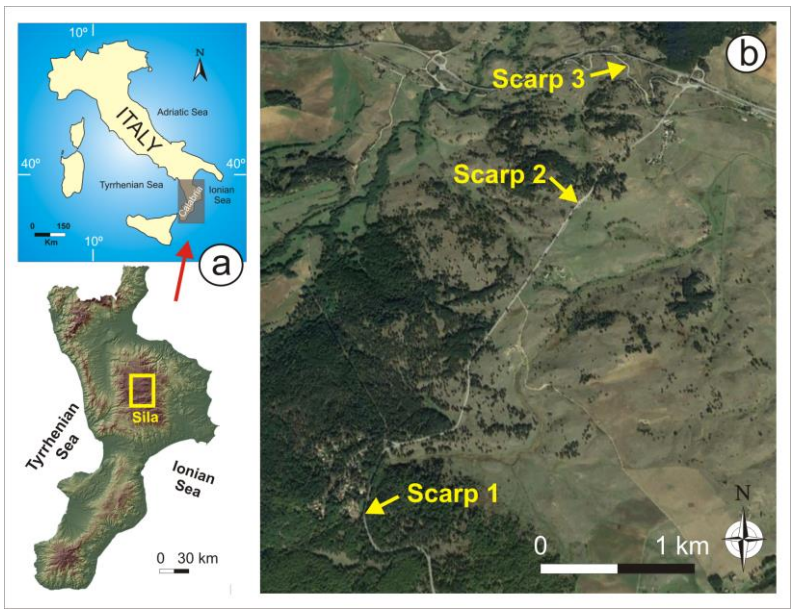

Fig. 1. Location maps of the study area (a) and of the three granodiorite scarps analyzed, reported on a Google Earth satellite image (b).

3.2 Field and laboratory assessment of weathering features

Field weathering features were assessed in the three scarps to evaluate the weathering grade classes according to the visual and physico-mechanical procedures proposed by Gullà and Matano (1997), in turn based on guidelines from the Geotechnical Engineering Office – GEO (1988) and partially revised by Scarciglia et al. (2016). Rock fabric, texture, colors and weathering patterns were described in detail. The resistance to rupture, scratching, indentation and acoustic response when using a geological hammer were evaluated on samples from each weathering class, along with local Schmidt hammer tests to measure the elastic rebound. The weathering profiles were classified into six classes and their transitions placed in the range between fresh (class I) to slightly weathered rock (class II), moderately (class III) to highly weathered (class IV) and completely weathered rock (class V) to soil and colluvial material (class VI).

From some representative rock samples, i.e. for classes with increasing weathering grades from I(-II) to VI, thin sections were prepared and observed under plane parallel (PPL) and cross polarized light (XPL) using a polarizing optical microscope to acquire more details on the weathering degree and patterns. Similarly, bulk samples of different weathering grade classes were observed by using a FEI Quanta 200 scanning electron microscope (SEM) equipped with an EDAX Genesis 4000 microprobe for energy dispersive spectrometry (EDS). EDS analyses especially contributed to the identification of the composition of Fe/Mn segregations and illuvial clay coatings, along with the major clay mineral assemblages based on Si/Al ratios and relative amounts of other cations (Mulyanto et al., 1999; Scarciglia et al., 2016).

The chemical index of alteration (CIA) was calculated to evaluate the degree of weathering of rock samples from the geochemical composition of the different weathering grade classes of the three scarps, according to the formula $Al_2O_3/(Al_2O_3 + CaO + Na_2O + K_2O) \times 100$ (expressed as molar proportions), where CaO is the amount found in silicate minerals only (Nesbitt and Young, 1982).

This ratio reflects the loss of labile cations such as Ca^{2+}, Na^{+} and K^{+} with respect to more stable, relatively immobile elements (Al^{3+}, Ti^{4+}) during weathering processes. To this purpose, X-ray fluorescence (XRF) compositional analysis of major elements (expressed as weight percentages of oxides) was performed on pressed powder disks of fine-grained milled, whole-rock samples by using a Bruker S8 Tiger spectrometer. Three replicates were measured to minimize errors by using international reference rock standards of the United States Geological Survey for data calibration. Total loss on ignition (LOI) was measured on an aliquot of the same samples after a 3 h heating treatment at 900 °C. The major elements were also used to assess possible changes in the chemical composition of the bedrock and/or controlled by weathering processes.

3.3 Laser scanning and post-processing

We collected scarp surveys by using a multitemporal approach, with yearly scans (T_0, T_1, T_2, T_3) in four consecutive years at the beginning of the winter season: 5th November 2015 (T_0), 17th November 2016 (T_1), 23rd and 24th November 2017 (T_2), and 9th November 2018 (T_3).

Instrument and conditions of measurements

Terrestrial Laser Scanner (TLS) technology is based on the time of flight of a laser pulse that starts from and returns to the instrument sensor after being reflected by an object. The distance range is combined with high-resolution angular encoder measurements to provide the three-dimensional location of a point (Hiremagalur et al. 2007). In this work, the TLS was located in front of the scarp to survey the whole object at once. However, the TLS position was not exactly the same for every year and, for scarp 1, the vegetation growth means that some areas in the point clouds are always in shadow.

The instrument used was a high-speed, high-accuracy TLS Leica HDS 3000 (Leica Geosystems, 2006), which was strategically positioned to cover as much surface as possible. Scan resolutions ranged from 10 to 30 mm in both horizontal and in vertical spacing to reproduce the scarp morphology. The data processing, performed using Cyclone© software (Leica Geosystems, 2006),

generated 3D point clouds composed of millions of points with the spatial resolution previously arranged. Each scan contained some high resolution control points (targets), whiche were measured by DGPS and used to georeference the whole point cloud for the multi-temporal overlap of 3D models.

Further data processing was achieved by using the open source CloudCompare software version 2.9 (Girardeau-Montaut, 2015). Vegetation on the ground surface was removed by using a filter tool (CANUPO), based on user-defined ground identification (Brodu and Lague 2012), and a "segment tool" to delete other unwanted points.

In order to distinguish whether the topographical changes between scarp models were scarp retreat or advance, we followed two different methods: the first method allowed assessment of the volume change and the mean retreat/advance rate of the whole scarp as the volume/surface ratio computed both yearly and between the first and the final survey (e.g., Hartmeyer et al., 2020); the second method allowed multitemporal changes pinpointed along each scarp surface to be detected by comparing just the first and last survey.

Using the "Compute 2.5D volume" CloudCompare tool, we computed the overlapping surface area and the volume between two subsequent rasterized point clouds. This tool counts on a rasterization process to produce a 0.25 x 0.25 m resolution grid by projecting the point clouds onto a plane, which is perpendicular to one of the main axes. The volume, is computed as difference in height between two different grids –multiplied by the total pixel area, and the surface area is calculated as the total pixels area. Since surface areas are different, volume differences are only computed on the matching pixels between grids (usually 85% to 95% of the total pixels) resulting in positive or negative value as consequence of weathering processes. An estimation of average scarp retreat/advance rates over each acquisition year and the whole period was achieved. Positive and negative values indicate mean net accumulation and mean erosion rates, respectively, spread over the whole scarp, i.e. obtained as volume divided by surface area (Hartmeyer et al., 2020).

The multi-temporal change detection was performed by using the "Multiscale Model to Model Cloud Comparison (M3C2)" plugin (Lague et al., 2013). This algorithm computed changes that

occurred over the whole scarp, highlighting areas of erosion and deposition by assessing the value of change in meters. In order to detect the changes, two georeferenced point clouds that were obtained at different times were overlapped and some corresponding point pairs were checked to improve the point cloud overlapping and refine superimposition. The accuracy of the measured distances was assessed by computing LOD95% (Lague et al., 2013), which represents the spatially variable confidence interval associated with distance measurements. This is derived from the combination of different sources of uncertainties, such as the position uncertainty of point clouds due to instrument precision, the registration errors between point clouds and surface roughness. The measured distance between two point clouds is more reliable where the detected changes are greater than the estimated errors. This evidence is highlighted as statistically significant change in the final model. The M3C2 and the 2.5D volume tools detect changes in only two point clouds at a time, thus they were applied to compare the year-by-year survey and the first and final point clouds acquired.

4. Results

4.1 Field features

The three granodiorite rock scarps display some distinct field features and weathering patterns (Fig. 2). Scarp 1 consists of dominant coarse-grained granite, whereas intermediate to fine grain sizes prevail in the other two scarps, with scarp 3 showing a very fine texture. Fresh (unweathered) and slightly weathered rocks, classified as weathering grade classes I and II, with null to very limited color and textural changes near the discontinuities, are very rare to absent along the three rock cliffs. Only felsic aplite dykes crossing the granitic bodies (Figs. 2a, c, e and 3a) of scarps 1 and 2 and some spheroidal boulders overlying the former, fully exhumed from the weathering profile at the topographic surface by erosion processes, and in some places having fallen or rolled down to its toe (Figs. 2a, 3b), belong to class I(-II) (cf. Scarciglia et al., 2016). Highly to completely weathered rock belonging to classes IV, V or VI and/or transitional grades (where changes in color towards brown, brownish yellow, yellowish red and reddish brown, and a loss of the original

texture/fabric and strength are progressively more pervasive) are common along the three scarps (Figs. 2, 3c).

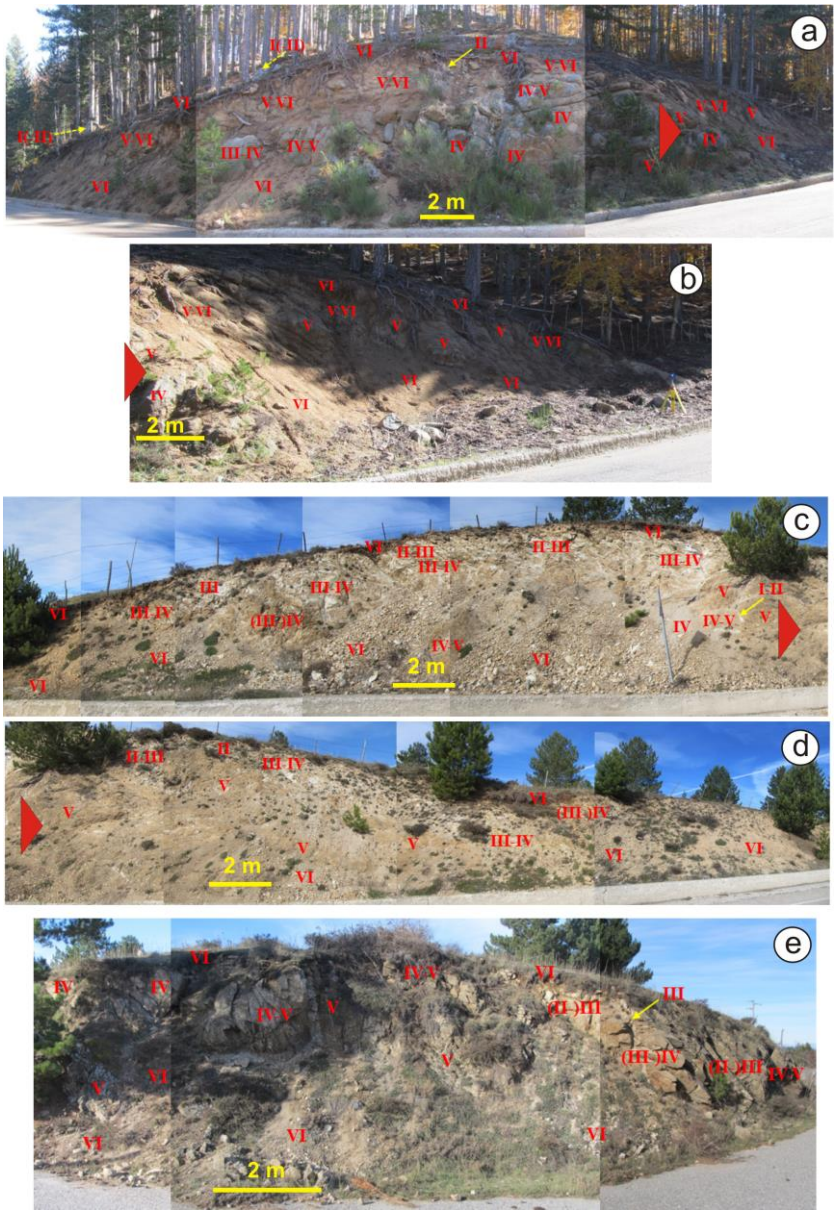

283 **Fig. 2**. Panoramic view of the three scarps analyzed: (a, b) scarp 1; (c, d) scarp 2; (e) scarp 3.
284 Large triangles indicate the lateral continuation of the scarp from one to an adjacent, partially
285 overlapping, image frame. Roman numerals refer to weathering grade classes. Arrows indicate
286 rounded boulders overlying scarp 1 and aplite dykes crossing the granitic bodies.

287

288 These weathering classes are coupled with less weathered classes III-IV or (III-)IV in the three
289 scarps and even class (II-)III or II-III and class III in scarps 2-3. Rock fractures are covered by
290 occasional to abundant iron (and/or manganese) oxyhydroxide segregations and clay coatings of
291 illuvial origin (Fig. 3c), which increase in the latter two scarps. Class VI consists of brown shallow
292 soils or colluvia close to the top of the three scarps (Fig. 3d) and slope debris at their foot (Fig. 3b).
293 A wider and more continuous talus, dominated by angular clasts (very coarse pebble to cobble in
294 size) with subordinate gritty debris and locally consisting of small detrital cones with their apex
295 corresponding to shallow bedrock incisions, was observed at the toe of scarp 2 (Fig. 3e). The
296 debris slopes of scarp 1, mainly located on its flanks, are dominated by finer granular detritus
297 (single crystal grains or lithic fragments from sand to fine gravel particles) (Fig. 3b), whereas this
298 material is alternated or mixed with large angular blocks on scarp 3, especially at the base of
299 widely jointed rock masses (Fig. 3f). Scarp 1 exhibits prevalent smooth joints and rounded to
300 subrounded corestones (cobble to boulder in size) that are included in the saprolite or are partially
301 exhumed. This a typical spheroidal weathering pattern, which often displays onion-like weathering
302 rinds affected by surface exfoliation (Fig. 3g). Conversely, rock joints in the other two scarps are
303 mostly planar with sharp angular edges, only showing poorly smoothed surfaces in places,
304 especially in scarp 3 (Fig. 3h).

Fig. 3. Major field features of the three scarps. (a) Fragmented remnants of whitish aplite dykes of weathering grade class I(-II) in the upper part of scarp 1. (b) Dominant fine granular detritus at the foot of scarp 1, along with some spheroidal boulders on its top and base. (c) Rock clast (class IV-V) from scarp 3 showing marked changes in color and consistency, with original texture and microstructure mostly present in relict form: primary minerals have lost their translucency and transparency, and are often separated or affected by microcracks; iron-manganese coatings widely cover rock surfaces. (d) Partially colluviated shallow soils trapped by tree roots on top of scarp 1. (e) Debris talus dominated by coarse angular clasts at the toe of scarp 2. (f) Jointed rock in the

upper cliff of scarp 3, with accumulation of large angular blocks at its base. (g) Rounded corestones within the saprolite, in places undergoing surface exfoliation of concentric weathering rinds. (h) Planar parallel sets of joints in scarp 3 separating rock masses into sharp angular blocks.

4.2 Micromorphological features

The analysis of thin sections confirmed the main differences in grain size in the granodiorite from the three scarps that had been estimated in the field. Scarp 1 mainly consists of large sialic mineral grains (quartz, feldspar and plagioclase), which are on average ≥ 3-5 mm in diameter, coupled with micas ≤ 1-3 mm (Fig. 4). Scarp 2 is very fine-textured, with grains that are usually ≤ 1-3 mm, among which micas are ≤ 0.5-0.7 mm. Scarp 3 exhibits intermediate grain sizes. Low weathering grade classes I(-II) and II exhibit higher (moderate to strong) etching and/or argillification of plagioclase than K-feldspar (Fig. 4a). Plagioclase is occasionally zoned, with the core showing severe pitting (Fig. 4a). Micas and chlorite are slightly etched, and rarely to occasionally show evidence of local clay neogenesis or iron oxidation (Fig. 4b). They often display partial separation, curved, wavy and/or split flakes along cleavage planes, especially at the edges, and the biotite appears chloritized, argillified and/or oxidized. Large biotite and/or chlorite (Fig. 4c) prevail over rarer and smaller muscovite in scarps 1 and 3 than in scarp 2, where, conversely, white mica is more abundant. Quartz and K-feldspar grains are also more abundant in scarp 2, than in the other two scarps, whereas higher amounts of plagioclase occur in scarp 1. In intermediate weathering classes, biotite (or chlorite) flaking, splitting and, sometimes, expansion at the edges are widespread and tending towards more weathered classes (Fig. 4d). Intra-grain fractures often propagate into surrounding quartz, feldspar and plagioclase grains (Fig. 4d). This results in a widespread physical breakage pattern of the whole rock with interconnected intra-, inter- and trans-granular, macro- and micro-cracks. In scarp 2, a dense network of closed microfractures appears which is widely filled with Fe-oxides and neogenic clay, mainly corresponding to very small biotite crystals affected by chemical weathering. Biotite (and, rarely, muscovite) exhibit slight to moderate oxidation and argillification, with further concentration and limited migration of Fe/Mn-oxides and/or clay coatings within the cracks of adjacent minerals (early stages of illuviation). Feldspar and

plagioclase show a high degree of corrosion (with rare exceptions) often leading to pseudomorphs. Even quartz appears slightly corroded in class IV and higher, in the three scarps (Fig. 4e), although this feature rarely occurs in scarp 3. In classes V and VI, most of the biotite and chlorite grains are largely oxidized and affected by in situ clay neogenesis, with some pseudomorphs (Fig. 4f). Both iron/manganese-oxide segregations and clay coatings extensively penetrate into surrounding mineral cracks (Figs. 4f, g). Mica flakes are often wavy and lead to exfoliation. The rock mass is widely fractured, creating a dense, interconnected network of open cracks and microcracks, occasionally filled with iron-oxides or clay coatings (Fig. 4d). Strongly to extremely etched and argillified plagioclase can be observed, coupled with poorly to extremely weathered K-feldspar. Quartz appears slightly to moderately corroded (Fig. 4g). In some places between close rock fragments and/or separated mica flakes, clayey and oxidized matrix patches occur, which show moderate anisotropic behavior between crossed polarizers (Fig. 4h). SEM observations of bulk samples confirmed all these features (Fig. 5). In addition, EDS microprobe analyses permitted estimation of the major clay mineral groups developed on weathered crystals or found in the illuvial clay coatings. Both 2:1 and 1:1 phyllosilicate clays were identified, independently of the weathering grade class. They range from vermiculite, smectite, illite and/or their mixed layers, where Si/Al ratios close to 2 are coupled with varying amounts of Fe, Mg, Ca, (Na) or K respectively, to kaolinite/halloysite, where Si/Al approaches 1 and other cations are absent to very scarce. Also, Fe/Mn- and occasional Al-oxides were detected.

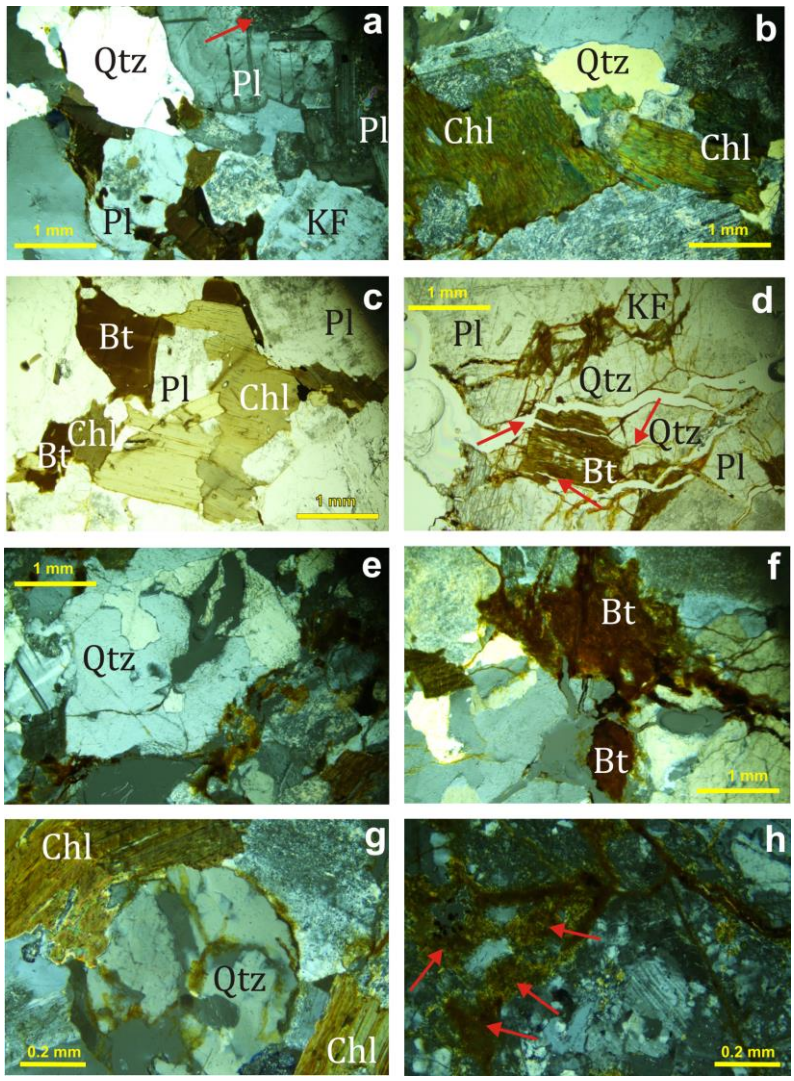

Fig. 4. Microphotographs of rock samples of different weathering grade classes in thin section. (a) Prevalent fresh to poorly weathered primary minerals, with plagioclase displaying moderate to strong etching and clay neogenesis, especially at the core of its zonation (arrow) (class I(-II), XPL). (b) Chlorite grains, with local clay neogenesis and iron-manganese oxide staining that are often parallel to cleavage planes or outer edges; locally curved flakes occur (class II, XPL). (c) Abundant fresh to slightly etched biotite and chlorite close to intensely etched plagioclase; chlorite exhibits weak flake separation and oxidation (class I(-II), PPL). (d) Highly weathered biotite affected by splitting and exfoliation of flakes along cleavage planes with crack propagation into surrounding quartz, feldspar and plagioclase grains (arrows); iron-manganese oxides and neoformed clays penetrate into the microcrack network (class V, PPL). (e) Slightly to moderately corroded quartz

(class (III-)IV, XPL). (f) Pseudomorphs of biotite pervasively affected by in situ neogenesis of clays and Fe-Mn oxides, which extensively penetrate into surrounding mineral cracks (class V, XPL). (g) Intense illuviation of clays sourced from weathered chlorite into cracks of weakly corroded quartz (class IV-V, XPL). (h) Development of Fe-Mn-oxide and clayey matrix patches with moderate anisotropic behavior (arrows) between mineral grain fragments (class VI, XPL). Abbreviations: Qtz: quartz; KF: feldspar, Pl: plagioclase; Chl: chlorite; Bt: biotite.

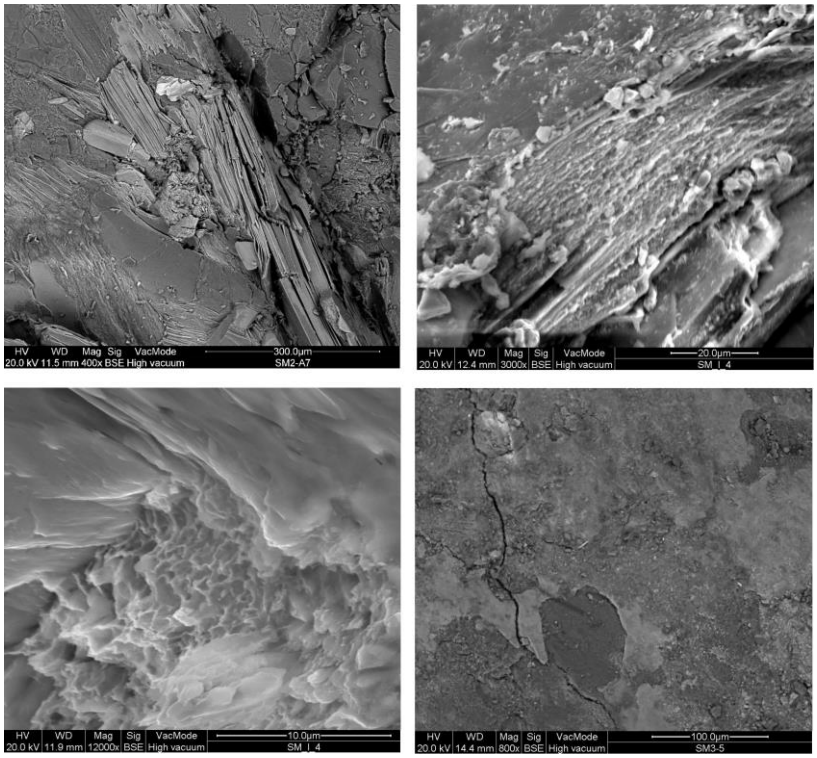

Fig. 5. SEM images of: (a) unweathered mica displaying partially curved and splitted flakes (class I(-II)); (b) in situ clay neogenesis on a mica grain (class IV); (c) deeply etched quartz grain (class IV); (d) illuvial clay coating widely overlying a mineral grain surface (class II).

4.3 Geochemistry

Mean values of the major element composition of the rock samples exhibit slight differences across the three scarps (Table 1). The standard deviation among replicates within each weathering grade

class is generally low and ranges from a minimum of 0.01 to a maximum of 0.81 for most oxides. Occasionally, SiO_2, Al_2O_3, Fe_2O_3 and K_2O are exceptions, with a standard deviation >1, up to 9.79, 2.69, 2.62 and 2.14 in classes VI and III-IV and II, respectively. Most of the weathering grade classes from the three scarps display mean CIA values of between 50 and 60. These data depict incipient to intermediate stages of chemical weathering in line with the classes proposed by Fedo et al. (1995). The degree of chemical weathering varies across the three scarps and is lowest in scarp 1 (mean CIA values = 55% as opposed to 57% and 60% in scarps 2 and 3).

Table 1

Mean values of major element concentrations expressed as weight percentages of oxides, loss on ignition (LOI) and chemical index of alteration (CIA) for different weathering grade classes from each scarp.

	SiO_2 (%)	TiO_2 (%)	Al_2O_3 (%)	Fe_2O_3 (%)	MnO (%)	MgO (%)	CaO (%)	Na_2O (%)	K_2O (%)	P_2O_5 (%)	LOI (%)	CIA %
Scarp 1												
I(-II)	64.89	0.88	14.47	5.71	0.09	2.05	3.04	2.72	4.21	0.32	1.08	50
II	67.70	0.41	14.98	3.00	0.04	1.09	1.87	3.31	4.74	0.15	2.58	52
(III-)IV	61.05	0.92	16.93	6.55	0.09	1.76	2.75	2.97	3.73	0.40	2.53	55
IV	70.01	0.27	15.46	2.18	0.04	0.93	0.71	2.79	5.96	0.09	1.81	56
V	66.09	0.42	16.51	3.23	0.05	1.07	1.25	2.80	5.56	0.15	2.65	56
VI	53.75	0.54	16.00	4.39	0.06	1.38	1.37	2.23	3.60	0.14	14.52	61
Scarp 2												
I-II	76.63	0.04	12.59	0.30	0.01	0.30	0.49	2.29	6.43	0.09	0.83	52
II	67.85	0.30	16.77	1.87	0.01	0.71	0.75	2.87	6.29	0.32	2.01	57
II-III	68.79	0.26	16.07	1.83	0.02	0.71	0.70	2.74	6.09	0.29	1.80	56
III	68.79	0.26	16.07	1.83	0.02	0.71	0.70	2.74	6.09	0.29	1.80	56
III-IV	63.44	0.41	18.21	3.89	0.03	1.75	0.55	1.16	7.00	0.18	3.44	63
IV	71.48	0.17	15.03	1.40	0.01	0.52	0.57	3.32	5.38	0.17	1.64	55
V	66.10	0.45	16.63	3.61	0.05	1.18	0.81	2.60	5.75	0.16	2.53	58
VI	65.10	0.32	17.02	2.52	0.05	0.88	0.62	2.45	5.24	0.24	5.02	61
Scarp 3												
III	69.84	0.08	17.34	0.94	0.02	0.42	0.75	4.04	4.59	0.32	1.30	57
(III-)IV	66.68	0.52	17.34	4.05	0.08	1.30	1.54	2.68	4.45	0.24	1.21	59
IV	64.03	0.60	17.48	4.56	0.09	1.47	1.32	2.79	4.25	0.21	3.22	60
IV-V	63.15	0.61	18.26	5.05	0.15	1.59	1.38	1.94	4.81	0.31	2.78	63
(V-)VI	59.70	0.47	15.58	3.72	0.07	1.10	0.99	2.25	4.34	0.19	11.35	60

4.4 Multitemporal scarp surveys

Data processing on TLS point clouds allowed detection of the surface changes that ~~-~~occurred on the three scarps over the period considered~~ (Table 2-)~~. The net volume change of each scarp (Table 2) ~~after each year of data acquisition (i.e. between two successive TLS surveys)~~ is computed as the difference in volume between the two 2.5D rasterized scarp surfaces assessed in ~~the~~ two successive surveys (cf. Kuhn and Prüfer, 2014): negative values represent a predominant loss of material (retreat) of the whole scarp, while positive values indicate a predominant deposition of sediments (advance). In the first period (2015-2016), both scarp 1 and scarp 2 show a negative value of net volume which indicates a marked material loss from the "scarp system". On scarp 3, this value is positive although very low. In the following time lapse, the volume is positive and increases at all sites: at scarp 1 and 3, the volume increase is more consistent in the 2016-2017 period than in the following, while the value at scarp 2 is greater in the final period than in the previous. A direct comparison between the first (2015) and the last survey (2018) shows that the total volume change assessed at scarp 1 is negative, whereas the values of the other scarps are positive, with lower values at site 3 than site 2. All these changes are expressed as the mean retreat/advance rate affecting the whole scarp by calculating the volume/surface ratio for each period.

Table 2. Changes in volume and surface assessed by the "Compute 2.5D volume" tool on all scarps, and scarp retreat/advance rates calculated as volume/surface ratios per year; grid spacing is 0.25 m. Surface values are different due to the size of shadow areas in each model.

	Scarp 1			Scarp 2			Scarp 3		
Time range (years)	Volume (m^3)	Surface area (m^2)	Retreat/ advance rate (mm ka^{-1})	Volume (m^3)	Surface area (m^2)	Retreat/ advance rate (mm ka^{-1})	Volume (m^3)	Surface area (m^2)	Retreat/ advance rate (mm ka^{-1})
2015-2016	-4.695	376.31	-1.3×10^4	-0.115	334.06	-3×10^2	0.370	137.88	3
2016-2017	1.448	381.56	4×10^3	1.200	334.31	4	1.077	142.63	8
2017-2018	0.240	380.00	1×10^3	2.011	333.69	6	0.540	144.00	4×10^3
2015-2018	*-3.894*	*379.50*	*~~-1 0~~3.4 x $10^{~~4~~3}$*	*3.054*	*333.63*	*~~9~~3*	*1.711*	*139.38*	*~~12~~4*

~~In order to~~To detect the effective topographical changes along the scarps and to check their accuracy on surface, a further processing was performed. The change detection tool (M3C2) computed the distance between points of two clouds~~,~~ but shows results as a Cloud of Difference (CoD): positive values indicate net sediment accumulation (advance) and negative values indicate loss of material (retreat), since the difference was calculated between the first (2015) and the final survey (2018). For all scarps, the CoDs (Figs. 6a, 7a, 8a) show positive values of distance. These are mainly in the lower sector of the scarps whereas the negatives are in the upper part. Most of the changes detected lie within a range of few centimeters (between +0.05 m and~~,~~ -0.05 m, with ~~the~~ most of the values around 0). The accuracy of data can be explored on the scarp model (Figs. 6b, 7b, 8b): it is not constant on the surface because it depends on different sources of error, and it ranges between 0.039 ~~to~~and about 0.045 m. It~~and~~ is visible as a significant change in CoDs (red in fig 6c, 7c, 8c), which show where the distance between the measured points can be considered reliable. Detailed topographical changes in each scarp are shown below.

Scarp 1

At the end of the survey period, changes were not statistically significant for most of the analyzed scarp surface (Fig. 6) since the CoD shows values that are lower than the distance uncertainty. In these areas, changes are negligible and so we consider these scarp portions as stable over the survey period. Nevertheless, the positive values of distance that are greater than the distance uncertainty (orange areas in Fig. 6a), which are the values that indicate deposition, are widespread on the right side of the slope and on the central left side, where visual observations in the field clearly indicated that sediments accumulate and the boulders are not visible. The negative values (light blue and blue areas in Fig. 6a), which indicate erosion and correspond to statistically significant changes, are located in the upper part of the slope: the highest value is for the central upper portion of the scarp and is probably due to a rock collapse.

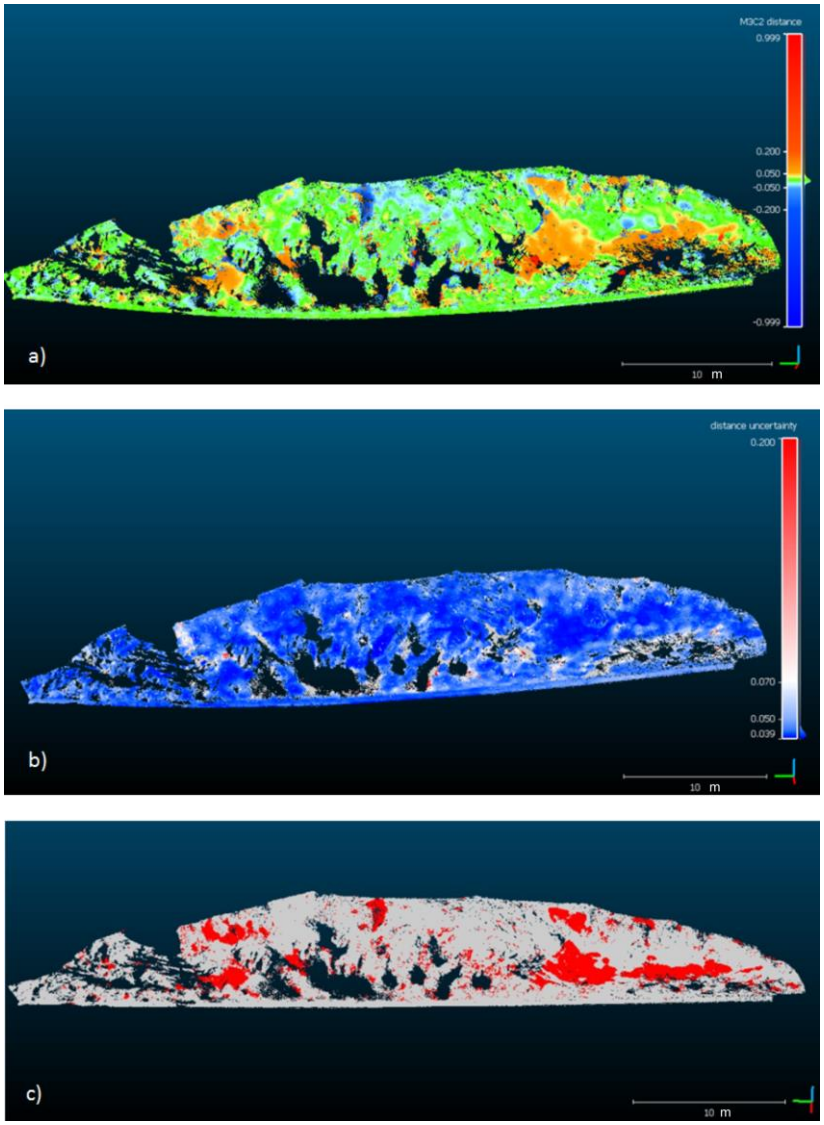

448

449 **Fig. 6**. Comparison between the 2015 and 2018 surveys of scarp 1: (a) CoD showing changes
450 detected through the M3C2 algorithm, positive values indicate deposition and negative values ~~of~~
451 ~~mean~~ erosion (measured distances are in meters); (b) distribution of distance uncertainty (in
452 meters) derived from the position uncertainty of point clouds due to instrument precision, the ~~with a~~
453 registration error of 0.02 m between point clouds and surface roughness (see section 3.3); (c)
454 statistically significant changes (areas of CoD values above the distance uncertainty) are in red,
455 whereas the areas in grey show where the confidence interval (distance uncertainty) is greater
456 than or similar to CoD values, and ~~; these areas~~they are considered as stable.

457

458 Scarp 2

459 The CoD shows that significant changes mainly occurred on the left side of this scarp (Fig. 7c).
460 The positive values (orange areas in Fig. 7a) mostly lie at the foot of the whole scarp, but rise in
461 the middle part of the slope on the left side. Here, the negative values (light blue and blue areas in
462 Fig. 7a) are also high and widespread, while they are much lower on the right side of the scarp. In
463 this part, almost all the changes are quite similar to the detected errors and so we consider these
464 scarp portions to be stable in the survey period.

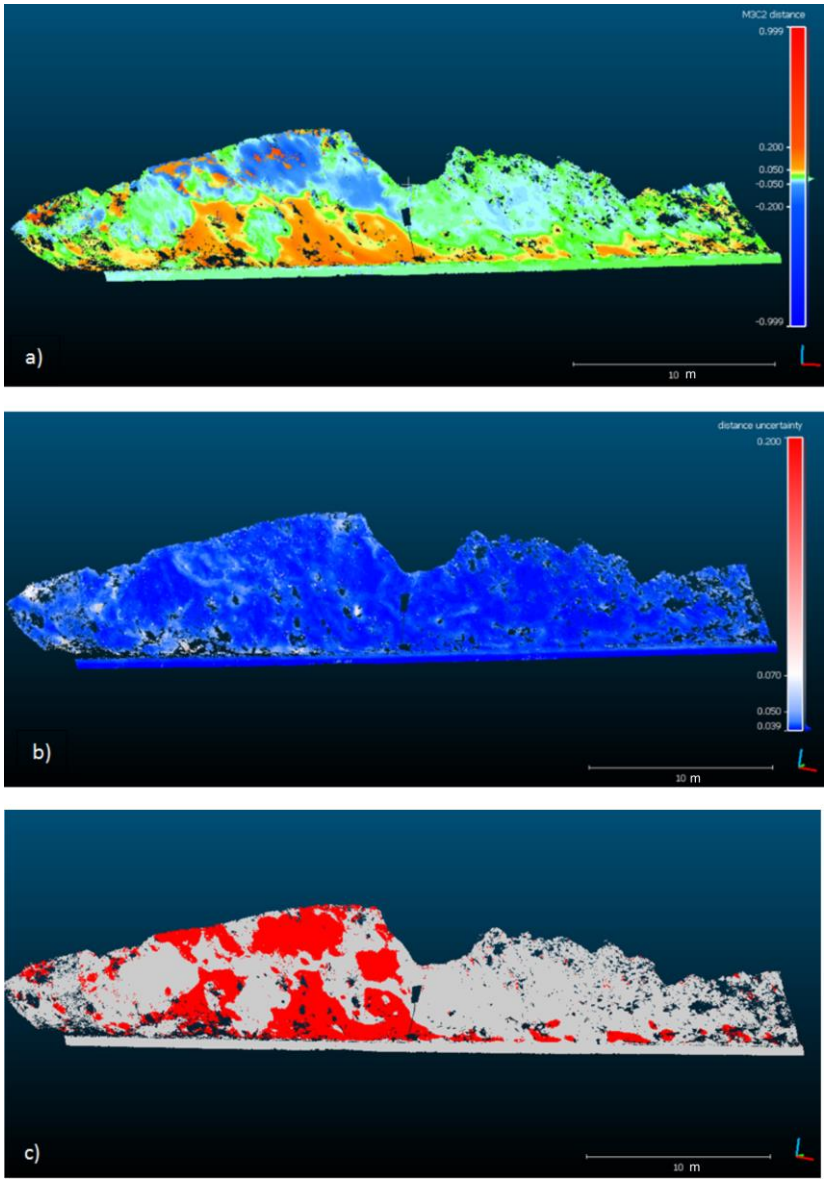

Fig. 7. Comparison between the 2015 and 2018 surveys of scarp 2: (a) CoD showing changes detected through the M3C2 algorithm, positive values indicate deposition and negative values ~~of mean~~ erosion (measured distances are in meters); (b) distribution of distance uncertainty (in meters) derived from the position uncertainty of point clouds due to instrument precision, the registration error of 0.02 m between point clouds and surface roughness (see section 3.3)~~with a registration error of 0.02 m~~; (c) statistically significant changes (areas of CoD values above the distance uncertainty) are in red, whereas the areas in grey show where the confidence interval

(distance uncertainty) is greater than or similar to CoD values, and ~~they~~; ~~these areas~~ are considered as stable.

Scarp 3

Changes are not homogeneous, given that they are scattered across the whole slope (Fig. 8c), while we consider most of the scarp stable for the survey period since the uncertainty linked to the error is similar to the CoD values. The significant changes with positive values (orange and red areas in Fig. 8a) are in the lower part of the scarp, whereas those with negative values (light blue and blue areas in Fig. 8a) are mainly found in the upper part. These latter are almost all significant in terms of value differences: the greatest change is visible on the right side of the scarp, where the highest negative values highlight a boulder collapse, that is clearly observed in the field.

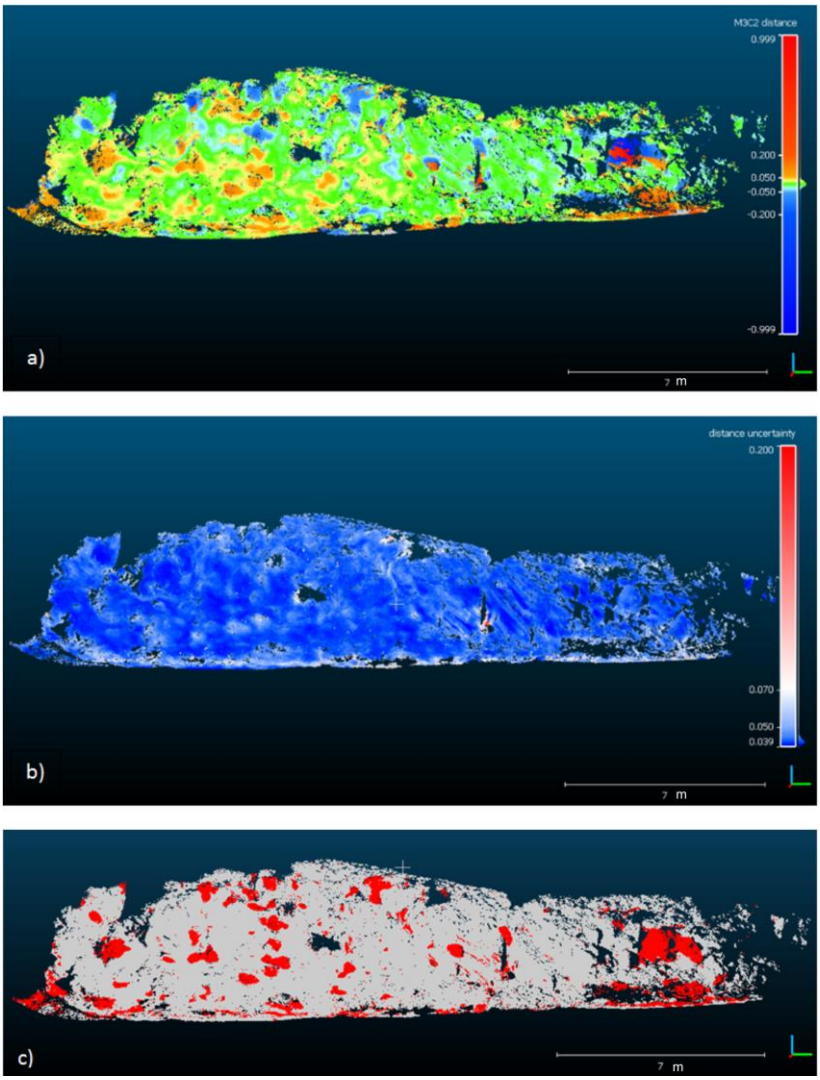

Fig. 8. Comparison between the 2015 and 2018 survey at scarp 3: (a) CoD showing changes detected through the M3C2 algorithm, positive values indicate deposition and negative values ~~of mean~~ erosion (measured distances are in meters); (b) distribution of distance uncertainty (in meters) derived from the position uncertainty of point clouds due to instrument precision, the registration error of 0.02 m between point clouds and surface roughness (see section 3.3)~~with a registration error of 0.02 m~~; (c) statistically significant changes (areas of CoD values above the distance uncertainty) are in red, whereas the areas in grey show where the confidence interval (distance uncertainty) is greater than or similar to CoD values, and ~~they; these areas~~ are considered as stable.

5. Discussion

5.1 Source lithology, weathering patterns and geomorphic processes

According to literature data, the major element composition of the rock samples from the three scarps is consistent with the granitic substrata outcropping in the study area (Messina et al., 1991; Liotta et al., 2008; Scarciglia et al., 2016). Average compositions across the three scarps with higher amounts of Fe_2O_3, Na_2O, CaO, MgO, TiO_2 and LOI in scarp 1, and lower quantities in scarp 3 which decrease further in scarp 2, are in line with the higher amounts of plagioclase, biotite and chlorite at the first site, along with the 2:1 clay minerals vermiculite and smectite (occasionally interlayered with illite), and iron oxyhydroxides. All these minerals are typical weathering products of the primary components mentioned above (Barnhisel and Bertsch, 1989; Sequeira Braga et al., 2002; Bétard et al., 2009; Apollaro et al., 2013), as already detected in the study area (Perri et al., 2015; Scarciglia et al., 2016). Conversely, the opposing trend of SiO_2 appears influenced by more abundant quartz in scarp 2. The apparent discrepancy between the increase in K_2O from scarp 3 to 1 and 2 and the amount of K-feldspar, suggests that K is also controlled by the abundance of primary micas and the neoformed product illite. Average Al_2O_3 content increases from scarp 1 to scarp 2 to scarp 3, with the same trend as the CIA index, suggesting that the increasing degree of weathering promotes important Al fixation in the crystal lattice of neoformed phyllosilicate clays (and/or Al-oxides) after its release from primary aluminosilicates. The contemporary occurrence of both 2:1 and 1:1 phyllosilicate clays in most of the samples suggests that the neogenesis of specific clay minerals depends largely on the intensity of the leaching processes (Taboada and Garcia, 1999a) at the local scale.

In all three scarps there is a great correspondence between the VI class as represented by the basal slope debris and the areas with high accumulation rates. The prevalence of loose granular detritus in the footslope of scarp 1 suggests the dominance of in situ grus production, a typical grain-by-grain disintegration process of coarse-sized rocks, including granite (e.g., Goudie, 2004), which is in line with the coarser grain size of the granodiorite at this site. Here, physical weathering due to insolation and frost cycles, i.e. thermoclastic and cryoclastic processes which are well-

documented in the Sila upland, likely enhanced by chemical weathering (e.g., Scarciglia et al., 2007, 2016), are consistent with present-day climatic parameters (Tables 1S 2S and 3; see section 5.2).

Table 1S

Mean monthly precipitation recorded at the weather stations closest to the study sites. Data from the Centro Funzionale Multirischi – ARPACAL (Calabria Region, Italy), available at url: www.cfd.calabria.it

Mean monthly and annual precipitations

Cecita

06_Nov_2013	***Dec-13***	***Juan-14***	***Feb-14***	***Mar-14***	***Apr-14***	***May-14***	***Jun-14***	***Jul-14***	***Aug-14***	***Sept-14***	***Oct-14***	***05_Nov-14***	***TOT***
190.2	*188.0*	*104.0*	*119.0*	*281.8*	*148.4*	*31.4*	*24.2*	*13.8*	*5.6*	*64.0*	*39.8*	*1.4*	*1212*
06_Nov_2014	***Dec-14***	***Juan-15***	***Feb-15***	***Mar-15***	***Apr-15***	***May-15***	***Jun-15***	***Jul-15***	***Aug-15***	***Sept-15***	***Oct-15***	***05_Nov-15***	
66.2	*78.6*	*139.4*	*172.6*	*242.4*	*34.6*	*46.8*	*24.2*	*47.6*	*64.4*	*96.2*	*217.0*	*2.6*	*1233*
06_Nov_2015	**Dec-15**	**Juan-16**	**Feb-16**	**Mar-16**	**Apr-16**	**May-16**	**Jun-16**	**Jul-16**	**Aug-16**	**Sept-16**	**Oct-16**	**16_Nov-16**	
97.6	1.4	81.6	92.6	145.4	36.6	64.4	75.0	31.2	121.6	126.8	125.8	103.4	1103.4
17_Nov-2016	**Dec-16**	**Juan-17**	**Feb-17**	**Mar-17**	**Apr-17**	**May-17**	**Jun-17**	**Jul-17**	**Aug-17**	**Sept-17**	**Oct-17**	**22_Nov-17**	
21.8	39.6	182.6	60.6	137.0	26.4	47.6	24.0	3.6	0.8	67.6	47.4	156.6	815.6
23_Nov-2017	**Dec-17**	**Jua-18**	**Feb-18**	**Mar-18**	**Apr-18**	**May-18**	**Jun-18**	**Jul-18**	**Aug-18**	**Sept-18**	**Oct-18**	**08_Nov-18**	
9.8	98.6	94.20	229.80	117.60	17.20	112.60	115.60	17.80	92.40	41.00	210.20	43.4	1200.2

Longobucco

06_Nov_2013	***Dec-13***	***Juan-14***	***Feb-14***	***Mar-14***	***Apr-14***	***May-14***	***Jun-14***	***Jul-14***	***Aug-14***	***Sept-14***	***Oct-14***	***05_Nov-14***	***TOT***
170.9	*189.6*	*131.2*	*160.2*	*320.0*	*174.6*	*35.0*	*32.8*	*14.4*	*1.6*	*59.2*	*48.6*	*0.2*	*1338.3*
06_Nov_2014	***Dec-14***	***Juan-15***	***Feb-15***	***Mar-15***	***Apr-15***	***May-15***	***Jun-15***	***Jul-15***	***Aug-15***	***Sept-15***	***Oct-15***	***05_Nov-15***	
65.6	*114.8*	*215.4*	*188.4*	*440.4*	*28.6*	*92.0*	*35.4*	*22.8*	*83.0*	*152.4*	*244.4*	*8.0*	*1691.2*
06_Nov_2015	**Dec-15**	**Juan-16**	**Feb-16**	**Mar-16**	**Apr-16**	**May-16**	**Jun-16**	**Jul-16**	**Aug-16**	**Sept-16**	**Oct-16**	**16_Nov-16**	
104.4	6.6	91.2	68.0	233.0	25.4	72.4	32.8	19.8	87.2	203.0	184.0	113.8	1241.6
17_Nov-2016	**Dec-16**	**Juan-17**	**Feb-17**	**Mar-17**	**Apr-17**	**May-17**	**Jun-17**	**Jul-17**	**Aug-17**	**Sept-17**	**Oct-17**	**22_Nov-17**	
41.8	39.6	294.6	89.2	212.4	43.2	18.8	0.2	4.8	0.4	88.4	26.4	225.2	1085.0
23_Nov-2017	**Dec-17**	**Jua-18**	**Feb-18**	**Mar-18**	**Apr-18**	**May-18**	**Jun-18**	**Jul-18**	**Aug-18**	**Sept-18**	**Oct-18**	**08_Nov-18**	
10.4	119.6	129.8	150.3	159.4	11.2	84.4	122.8	23.2	55.4	37.8	288.2	41.2	1233.7

Table 2S.

Daily temperatures, with no. of days with freeze-thaw cycles and frost cracking window. Raw data from the Centro Funzionale Multirischi – ARPACAL (Calabria Region, Italy), available at url: www.cfd.calabria.it**Table 3.**

No. of days with freeze-thaw cycles and frost cracking window over each data acquisition year, over the entire acquisition period and over the entire period with 2 preceding years, and corresponding average values.

Commented [1]: Due to its very big size this new Table (which includes different data from the previous Table 2S) is not included in the text, but can be downloaded from the Editorial Manager platform of the Journal.

Table 3. No. of days with freeze-thaw cycles and frost cracking window over each data acquisition year, over the entire acquisition period and over the entire period with 2 preceding years, and corresponding average values

Time intervals	NOV 2013 - NOV 2014	NOV 2014 - NOV 2015	NOV 2015 - NOV 2016	NOV 2016 - NOV 2017	NOV 2017 - NOV 2018	NOV 2015 - NOV 2018	NOV 2013 - NOV 2018	Average NOV 2015 - NOV 2018	Average NOV 2013 - NOV 2018
No. of days with potential freeze-thaw cycles	121	67	75	66	73	214	402	71	80
No. of days with frost cracking window	37	65	33	55	59	144	246	49	50

The spheroidal weathering pattern (partly inherited from deep weathering in the past; e.g. Scarciglia, 2015) and the pervasive change in color/fabric of most of the granodiorite outcrop testify to chemical processes acting as predisposing factors for rock flaking and granular breakdown. Migoń and Vieira (2014) showed that coarse-grained granite is more prone to rock surface smoothing and rounding, which lead to typical spheroidal corestones and make rock masses more susceptible to water-controlled weathering mechanisms. The widespread crack network observed in the samples from scarp 1 at the microscale, partly radiating from split and expanded flakes of biotite into surrounding mineral grains (Isherwood and Street, 1976; Taboada and García, 1999b), supports the idea of an active role of this rock breakage pattern in the enhancement of the above-cited weathering processes (Goodfellow et al., 2016), together with an upscaling effect (Viles, 2001; Scarciglia et al., 2007). This is consistent with the findings of Vierra et al. (2018), who suggested that the weathering of biotite (with its expansion due to vermiculitization) is the primary driving force in the formation of spheroidally weathered corestones in Mediterranean climate conditions. Furthermore, surface curvature may cause an increase of tensile stress normal to rock surface (Martel, 2006). The VI class patches close to the top of the scarps, where soils and colluvia

occur, surprisingly appear to be classifiable from highly eroded to stable up to affected by deposition. The erosion pattern is consistent with highest weathering grades of the rock, so leading to high amounts of loose mobile material. Common erosion zones corresponding to the V-VI class masses, especially along scarp 1, confirm this behavior. Nonetheless, scarp 2 shows large areas affected by intense erosion even in the lower weathering grade classes II-III, (III) and III-IV, where physical fracturing of the bedrock prevails over its chemical weathering. This finding is consistent with the wider debris slope with angular rock fragments (rather than loose granular material) at the toe of this scarp than at that of the other two. Prolonged snow patches (Fig. 9a) and cryonival processes (mainly topsoil, ground-surface or marsh freezing in places creating earth-hummocks) confirm the role of ice and thermal stress during the winter/spring seasons (see section 5.2). Migoń and Vieira (2014) supposed that very fine texture of the granodiorite acts as a further control on such angular rock shapes, which is consistent with what we found at scarp 2 and in line with the frequent, still closed microcracks observed in the thin sections. The scarcity of large biotite and chlorite crystals, coupled with the occurrence of fine-grained muscovite, likely hamper the effects of crack propagation from exfoliated micas to adjacent mineral grains, thus preventing major grain-by-grain rock disintegration. A volume increase indicating accumulation observed on the top of the scarps suggests some external feeding of colluvial material from upslope, sometimes trapped by the tree root network. In some cases, our data display a local coupling of zones with high erosion rates adjacently to others with high accumulation rates, which often indicates short-distance transport of the eroded material along the scarps. Where jointed rock masses or isolated blocks were observed in the field (mainly along scarp 3 and, subordinately, scarp 2), this coupled erosion/accumulation pattern suggests a pre-failure deformation. In other words it might be a precursor to potential gravity-driven phenomena such as rockfalls (Abellán et al., 2010) and a basis for timely prediction and prevention of landslide hazards and risk (Rowe et al., 2018; Fanos et al., 2019). A simple tilting of rock blocks prior to falling/toppling simulates (but does not really represent) net accumulation. This interpretation is confirmed by the identification of deep, wide cracks affecting large rock masses along scarp 3 in 2017 (Fig. 9b), which led to the detachment of large rock slabs and accumulation at the scarp toe (Fig. 9c) or further divarication of other rock

588 blocks in 2018 (Fig. 9d). Erosion is localized in small, mostly isolated, patches of V and IV-V
589 weathering grades, where partial granular decomposition occurs, but also in small, less weathered
590 rock portions of classes (II-)III and (III-)IV. Rock texture seems to control the main weathering
591 patterns. The granodiorite substratum with intermediate grain sizes at this site explains the
592 coexistence of angular physical breakage patterns with local rounding (Migoń and Vieira, 2014)
593 and grussification. The latter appears to be partly controlled by the dominant mineralogy, where
594 biotite (and chlorite) largely prevail over white mica and undergo some flake divarication and
595 splitting.

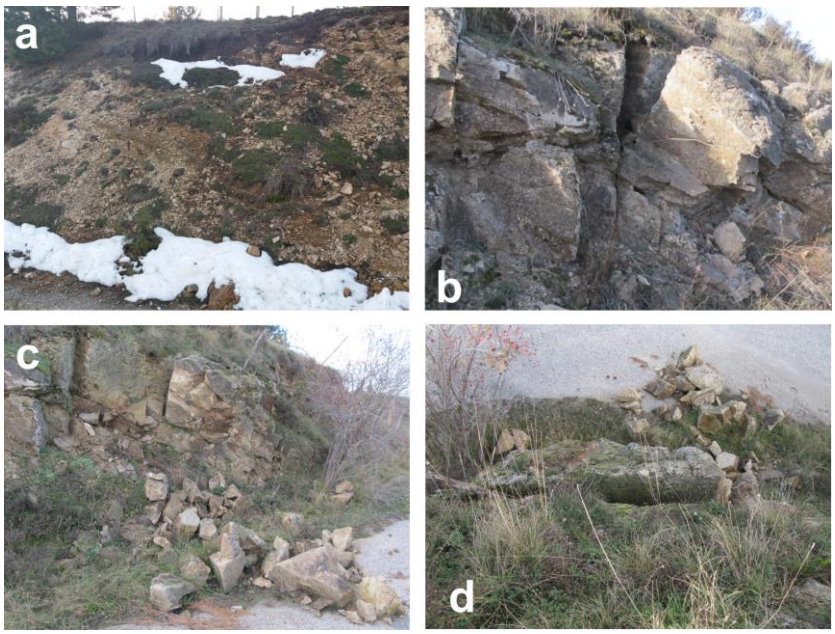

596

597 **Fig. 9**. (a) Snow patches along scarp 2 during the spring season. (b) Deep rock cracks separating
598 and tilting large rock blocks of scarp 3 as potential precursors to rock falls/topples (2017). (c)
599 Rockfall accumulation at the toe of scarp 3 (2018). (d) View from the top of scarp ~~2~~3 of another
600 open crack separating a large unstable rock slab from the main cliff (2018).

601

602 In addition to textural and mineralogical properties, the varying spatial distribution of weathering
603 features and grades in the three scarps suggests that such patterns are controlled at the local

scale by microclimatic conditions (e.g., even small differences in insolation and moisture content), which are, in turn influenced by slope aspect. The prevalence of high weathering grade classes along scarp 1 is consistent with its W-facing aspect, as it is in shadow for longer periods and favorable to prolonged moisture availability because of less daily insolation. In turn, these conditions promote intense and pervasive chemical weathering processes, such as hydrolysis, reduction/oxidation and dissolution. The presence of pine forest cover (unlike the other two scarps) likely helps maintain moister conditions over time and mitigates thermal excursion. Furthermore, greater grus production and basal accumulation could be related to overall lower temperatures due to shorter insolation and to a tendency to freeze-thaw cycles. Daily temperature values during the coldest months (Table 2S; see section 5.2) indicate the recurrence of freeze-thaw cycles (Table 3) and consequent cryogenic production of granular debris. Such interplay between intense chemical and physical degradation processes may explain the apparent inconsistency between the overall lowest degree of chemical weathering indicated by the CIA index and the prevalence of higher weathering grade classes estimated through visual and mechanical tests. Scarciglia et al. (2016) already remarked upon such potential discrepancy between data obtained from geochemically- and physically-based methods on the granitic substrata of the Sila Massif, due to a possible decoupling of chemical weathering and physical breakage processes, which, in turn, is derived from the different action and intensity of these two types of rock degradation and their effects on rock strength. The highest erosion rates on scarp 1 indicate high efficiency in the mechanical removal of weathered, loose and mobile material. Despite the forest cover, a much longer and steeper hillslope over this scarp likely promotes greater water runoff, surface wash and soil creep processes from upslope. Shallow topsoils, tearing of the soil/grass cover, seasonal removal of the abundant litter, surface stoniness, local exposure of tree roots and bare bedrock/saprolite at the topographic surface, support this hypothesis. The SE-facing aspect of scarp 2, coupled with overall lower weathering grades of the rock exposed, suggests a more temporary availability of moisture controlled by prolonged insolation, with water mainly infiltrating within rock joints rather than penetrating deeply into rock cores through surface micropores. Intermediate values of CIA are in line with an abundance of intermediate weathering grade classes. Nonetheless, the highest values

of this index in the transitional class III-IV, rather than in the most weathered classes, are surprising and apparently inconsistent. Indeed, the clay and iron/manganese-oxyhydroxide pedofeatures identified there produce an apparent overestimation of the degree of weathering. This can be easily explained by the fact that there are also illuvial processes (Scarciglia et al., 2016). The local microclimate conditions are likely favorable to seasonally varying diurnal freezing cycles (see section 5.2) that are able to produce coarse angular clasts from the breakdown of less chemically weathered, fractured rock. Somewhat similar features observed on scarp 3 coexist with locally pervasive chemical weathering and granular disintegration. These findings indicate microclimatic conditions that are midway between those affecting the other scarps and which relate to the varying, E to NE-facing aspect of this cliff. Here, the CIA is on average higher than at the other sites, but the two sectors with varying aspect display some differences. The rock masses that exhibit the lowest weathering grade classes prevail on the NE-facing side, less exposed to insolation, whereas the most weathered classes occur in the eastern sector, where the role of moisture seems to be more relevant. The more prominent role of gravity-driven processes such as rockfalls, along this scarp and scarp 2, appears to be controlled by rock jointing rather than aspect and microclimate. The presence of abundant illuvial features in some weathering grade classes of the same scarps, despite their east-facing exposures, suggests that their translocation downwards was a process that was partly inherited from past conditions of formation. This is in line with: (a) higher CIA values in the samples of these scarps, which likely overestimate the in situ chemical weathering (see above); (b) the current lack of proper soil profiles with horizons rich in clay fraction and iron-bearing primary minerals overlying the weathering profiles (except for shallow organic-rich topsoils), which should have sourced Fe/Mn ions and fine particles; (c) the overall coarse-textured granodiorite parent rock with no primary clay particles (cf. Scarciglia, 2015; Scarciglia et al., 2016); (d) the etching of quartz grains, which is likely due to hundreds of thousands of years of exposure to chemical weathering of some (cf. Scarciglia et al., 2015).

5.2 Scarp retreat rates, weathering and climate

Most of the analyzed scarp surfaces did not show statistically significant changes over the three years. Nonetheless, the evidence that (a) the zones characterized by significant values correspond to those affected by higher accumulation or erosion (also detected visually in the field), and (b) those with values of CoD lower than the distance uncertainty can be assumed as overall stable during the time interval of data acquisition, i.e. without relevant yearly changes, suggests that average rates of scarp retreat/advance are reliable. Actually, the erosion rates provided in this study are consistent with literature data obtained both in the same area and elsewhere through other methods (see below). The comparison of the behavior of the three scarps during the whole survey period shows that only scarp 1 recorded a net loss of rock volume, clearly pointing to erosion of the weathered material. However, this scarp and scarp 2 experienced an initial phase of erosion (2015-2016) alternated with more prolonged phases of volume increase indicating deposition (2016-2017 to 2017-2018). Conversely, a continuous (although very low) gain in volume in scarp 3 over the whole time period highlights dominant accumulation. These findings suggest that after the removal of abundant loose material in the first period, the first two scarps were less prone to erosion and that this might shift from transport-limited to transient weathering-limited conditions. The three scarps behave as open systems that are strictly linked to the entire hillslope, where they received mobile material from upslope and this was, at least temporarily, stored until new erosive events would remove it from the sites. The high erosion rates in scarp 1 are consistent with its more severe grussification and production of loose granular debris. Occasional rockfalls on scarp 1 (and, to a lesser extent, on scarp 3) also appear to be triggered by biomechanical weathering promoted by tree root deepening and wedging into granite cracks, with further breakage and comminution of detached blocks (Scarciglia et al., 2007). In contrast, scarce to null net erosion occurred on the other scarps, where more limited grain-by-grain disintegration is coupled with coarser rock fracturing and mass wasting processes. Although the three scarps are located along road cuts, we can assume that this does not greatly affect largely the estimated erosion/accumulation rates. Indeed, several natural scarps displaying comparable heights, aspects and weathering features/processes occur in the Sila upland landscape (see section 3.1) and traffic is very light there. An occasional maintenance cannot be excluded, but it mainly involves the road

surface. It may especially affect just the hillslope overlying scarp 1, although is very limited over time. Indeed, at the base of scarps 1 and 2 there is a varying empty space behind the road, about 1-2 m in width, which easily accommodates the detritus produced from their weathering and retreat. Very rarely, a small part of such detrital material bypasses this space to reach the adjacent road. The road at the base of scarp 3 is a minor track and thus extremely poorly busy. Both rockfall blocks and snow cover lie there for weeks or even months, as directly observed during repeated field surveys over several years (even preceding and following the current TLS acquisitions). No removal of unstable rock blocks is performed in advance from this scarp.

During the first and third periods of observation (2015-2016 and 2017-2018), mean annual precipitation was higher than in the intermediate time range (Table 1S), but no specific trends or relationships are evident between this climatic parameter and the estimated erosion/accumulation rates. Only scarp 1 responded with higher erosion rates during both the first time range and the whole period of data acquisition, confirming easy mobilization of the weathered material, in line with an abundant granular disintegration enhanced by physical breakage processes observed at this site. Not even mean annual temperatures exhibit any apparent direct connection with redistribution rates. Nonetheless, daily temperatures over the three yearly periods, and especially oscillations of a few degrees around 0 °C during the coldest months, likely triggered freeze-thaw cycles, which promoted this in situ grussification through frost shattering, especially (but not exclusively) at the first site. In particular, 214 potential freeze-thaw cycles occurred from November (and occasionally from October) to April (with rare events in May) over the entire acquisition period, with an average of 71 events per year (Tables 2S and 3). For 144 days, the daily temperatures fell to within the so-called “frost cracking window” (ranging between −3 °C and −8 °C), which is considered particularly favorable for ice lens growth and frost cracking (Anderson et al., 2019). Actually, stable to slowly changing thermal environments appear more prone to the rock cracking process than those with abrupt fluctuations in surface temperature (Rempel et al., 2016). Although the potential role of thermoclastic processes is difficult to assess on the basis of the climatic data available (Table 2S), a temperature change (ΔT) of ≥ 8−10 °C occurred on some days in almost every month, occasionally on up to 25-30 days during some of the warmest or coldest months.

Maxima daily ΔT of up to 15.3 °C occurred in April 2018, whereas monthly ΔT were mostly ≥ 18−20 °C over the entire period and reached a maximum of 30.2 °C in May 2015. Recent work has indicated that rates of temperature change of much lower magnitude than the 2 °C min−1 threshold commonly assumed necessary for cracking by thermal stress (Boelhouwers and Jonsson, 2013) could trigger cracking and rock fatigue. Diurnal thermal cycles induced by insolation may cause subcritical crack growth (a process driven by a magnitude of stress loading that is lower than a rock critical strength, such as tensile or compressive strength; Eppes et al., 2018) even in mid-latitude humid temperate climates (Aldred et al., 2016). Subcritical cracking has a progressive, cumulative effect on rock dilation changes and fatigue over time (Eppes et al., 2016; Lamp et al., 2016) and is a dominant process of mechanical weathering and rock erosion (Eppes et al., 2018). Whatever the source of the stress (e.g., freeze-thaw or thermal cycles), climate seems to play a prominent role in controlling subcritical cracking and weathering rates (Eppes and Keanini, 2017). Thermally induced stresses have greater magnitudes as crystal size increases and are largely controlled by mineralogical differences within the rock (Anderson et al., 2019), because of the different albedos of dark- and light-colored crystals (Gómez-Heras et al., 2006) and varying thermal expansion coefficients. The differential thermal responses of adjacent minerals ~~is~~are efficient in granite at the microscale, leading to surface cracking and granular disaggregation. Scarp 2 was also affected by general erosion over the 2015-2016 time interval, but nonetheless experienced a net accumulation over the total three years. Scarp 3 recorded the lowest net positive change in volume from 2015 to 2018, with net accumulation occurring in the three yearly time lapses. To explore how the scarp systems responded to erosion and accumulation processes, notwithstanding the lack of connection with precipitation and temperature patterns, the climatic conditions were also investigated for the two years before T_0. Over this time range, mean annual precipitation was higher than that for each year within the studied period. This finding confirms that rainfall did not influence either the (higher) erosion rates detected at the first two sites or the accumulation rates. Only values of mean annual precipitation below those for the 2015-2018 interval would have promoted a temporary storage of potentially mobile debris during the previous two years, followed by its relevant erosion at the beginning of the studied period. However, during

743 the preceding two years the number of potential freeze-thaw cycles was particularly high (189),
744 almost doubling those recorded during the whole data acquisition period with up to 121 cycles
745 during the first year. Up to 65 days in the second year intersected the “frost cracking window”. This
746 suggests that cryogenic processes before T_0 acted as a major predisposing factor of the
747 erosion/accumulation dynamics that occurred after T_0. This could easily have caused physico-
748 mechanical breakdown of the granitic rocks and made mobile material liable to water runoff and
749 gravity-driven phenomena.

750

751 *5.3 Comparison of scarp retreat rates with literature data*

752 The data for scarp retreat rates in granitic mountainous landscapes available in the literature are
753 poor. Most are assessed for a variety of sedimentary rocks, including volcanic deposits, under cold
754 semi-arid to hyper-arid (hot desert), subtropical and polar climatic conditions, and range from 0.006
755 to 10, with one surprising (unlikely) value of 200 m ka^{-1} (Matmon et al., 2005; Siewert et al., 2012;
756 Finzi and Harlev, 2016; Duszyński et al., 2019).

757 The retreat/advance rates of the three scarps in the Sila upland are always very low and range
758 from n x 10^{-6} to 10^{-2} m yr^{-1} (equivalent to n x 10^{-3} to 10^{1} mm yr^{-1} or n x 10^{0} to 10^{4} mm ka^{-1}). If only
759 net erosion rates are considered, the range is between 1 x 10^{-2} and 3 x 10^{-4} m yr^{-1}. These values
760 are of the same to two orders of magnitude slower than the average exhumation rates estimated
761 with ^{10}Be in the same study area (Raab et al., 2018), which range from about 0.036 to 0.062 mm
762 yr^{-1} (equivalent to 3.6-6.2 x 10^{-5} m yr^{-1}), with a maximum of ca. 0.40 mm/year (4 x 10^{-4} m yr^{-1}).
763 However, the data from cosmogenic beryllium refer to rates of surface lowering, which exposed
764 tors and boulders from the saprolite over the last ~100 ka (Raab et al., 2019). Therefore, they
765 record rates averaged on long-term geomorphic processes and climatic cycles rather than high
766 frequency, yearly to shorter (seasonal, monthly, etc.) climate shifts. They include different
767 geomorphic responses over time controlled by major climate and vegetation changes, with phases
768 of very scarce to almost null erosion during the Last Glacial Maximum (when debris production
769 likely prevailed in response to freeze-thaw cycles and thermal stress), followed by a marked

increase in erosion rates during the transition to the early (and partly middle) Holocene. This can be explained by the great amount of debris made available after the physical weathering of the local bedrock in the glacial stage, easily mobilized by the increasing rainfall and moisture availability during the post-glacial transition. Medium-high scarp retreat rates are also comparable to the short-term soil erosion rates of ~1.23 mm yr^{-1} (1.23 x 10^{-3} m yr^{-1}) calculated ~~as~~ through fallout $^{239+240}Pu$ isotopes for the last ~50 years (Raab et al., 2018). Average erosion rates (~0.09 to 0.13 mm yr^{-1}) estimated in river sediments for the low-relief upland landscape of the Sila Massif using cosmogenic ^{10}Be constitute partly overlapping orders of magnitude (Olivetti et al., 2012).

In the central European Alps, Hartmeyer et al. (2020) estimated a recent retreat rate of a cirque wall in schist, which hosts an active glacier, of 1.9 mm yr^{-1}. Curry and Morris (2004) estimated present-day rates of scarp retreat (0.014 mm yr^{-1} = 1.4 x 10^{-5} m yr^{-1}) and talus accumulation (0.022 mm yr^{-1} = 2.2 x 10^{-5} m yr^{-1}) from rockfall processes affecting sandstone in Wales. The authors showed that these rates are two orders of magnitude slower than those estimated for the Lateglacial (1.01-2.44 m ka^{-1} or mm yr^{-1}), which they tentatively assumed as valid for Pleistocene glacials. Within the latter, which are in turn one order of magnitude faster than rockwall retreat rates during the Holocene (0.10 to 0.17 m ka^{-1}), a contribution of retreat by rockfall (0.64 to 1.67 m ka^{-1}) can be separated from that driven by granular weathering due to microgelivation (0.35 to 0.77 m ka^{-1}). Although calculated on a different lithology, these findings suggest that the scarp retreat rates estimated in this study are generally much slower than the long-term denudation rates obtained by Raab et al. (2019), because microgelivation very likely plays a lesser role at present than during the last (and, possibly, past) glacial stages. Conversely, during the Last Glacial stage microgelivation presumably acted as a major source of loose debris production (as a response to increased freeze-thaw and diurnal insolation cycles and their persistence over time) which was, in turn, prone to erosion at the onset of the Holocene climate amelioration. Nowadays, rockfalls appear as prominent key processes in cliff retreat, especially in scarps 2 and 3, although cryoclastism and thermoclastism seem to make a clear contribution, particularly in scarp 1.

A further comparison of the current scarp retreat rates with worldwide literature data shows that they fall within the range of long-term denudation rates (0.001-0.25 mm yr^{-1}) estimated from granite rocks in cold (alpine) to cool temperate environments (Small et al., 1997; Riebe et al., 2000; Granger et al. 2001; Heimsath et al., 2001; Phillips et al., 2006; Egli et al., 2010; Gunnell et al., 2013; Scarciglia, 2015). Exposure of schists also proceeded at partly comparable rates of 0.02–0.2 mm yr^{-1} in semi-arid climatic conditions of New Zealand (Raab et al., 2021). By using cosmogenic ^{10}Be in the quite different hyper-arid desert environment of the Namib, Matmon et al. (2013) estimated average cliff retreat rates on a granite inselberg of about 8 mm ka^{-1} over the last $>10^5$ years, whereas the corresponding lowering rate of the bedrock (~1–2 mm ka^{-1}; Bierman and Caffee, 2001) was up to 2–3 times slower. The data obtained in our work are conversely 2 to 4 orders of magnitude slower, probably because extreme thermal cycles leading to rock fatigue and fracturing are more efficient in the desert than in the Sila cold temperate environment.

6. Conclusions

This work has provided data that contribute to the understanding of the major relationships between field (macroscale) features, microscale minero-petrographic data, geochemical properties including weathering textures, relief features and short-term scarp evolution in a Mediterranean mountain environment. Intermediate to high weathering grade classes dominate in three granodiorite scarps that were studied in detail, with meaningful differences in grain size and slope aspect. These properties appear to control the formation of rounded (coarser-grained granite with larger biotite and chlorite crystals, moister and less insolated) rather than angular (finer grained, more insolated with temporary moisture availability) weathering patterns. Corresponding fine versus coarse sizes of the weathered material detached from the bedrock are, in turn, facilitated by prevailing chemical or physical rock degradation processes. Apparent inconsistencies between CIA values obtained for the three scarps and the weathering grade classes prevailing therein are due to different extents of mechanical rock breakdown, on occasions_exceeding chemical attack, or illuviation of neoformed clays and Fe/Mn oxides. Rock jointing rather than aspect and microclimatic

conditions likely control rockfall processes, in some cases enhanced by the biomechanical action of tree roots penetrating into granite cracks. On the other hand, root networks show their efficiency in hampering surface erosion by partially trapping topsoils.

An initial assessment of three-year surface and volume changes due to cliff evolution (erosion and accumulation) by using terrestrial laser scanning for the period 2015-2018 was carried out. An attempt to estimate average rock-retreat rates was performed through a comparison of 3D models that were reconstructed from the yearly TLS surveys. Our quantitative results are consistent with literature data and contribute to a better understanding of current geomorphic dynamics, including pre-failure landslide processes, which affect the scarps, and their relationships with weathering features, patterns and grades. Further data acquisitions using multiannual time slices are planned in the near future to minimize inherent acquisition errors and obtain more reliable quantitative retreat rates.

The integrated approach proposed in this work provides new insights into the properties of fragile weathering/soil mantles in mountain ecosystems, often threatened by ongoing and future climate changes, and might be a basis for the assessment and management of geomorphological hazards and associated risks in a range of climatic environments.

Acknowledgements

This research was partly funded by MIUR (Ministero dell'Istruzione, dell'Università e della Ricerca), through ex-60% Projects at Università della Calabria (grants to F. Scarciglia). We are grateful to M.M. Piane and C. Zumpano for some laboratory analyses and to M. Davoli and G. Niceforo (DiBEST, University of Calabria) for their assistance in SEM-EDS and XRF analyses. Many thanks are due to two anonymous reviewers, whose constructive comments and suggestions greatly helped improve the manuscript quality, and to Martin Brimble for his revision of the English.

References

Abellán, A., Calvet, J., Vilaplana, J.M., Blanchard, J., 2010. Detection and spatial prediction of rockfalls by means of terrestrial laser scanner monitoring. Geomorphology 119, 162–171.

Aldred, J., Eppes, M.C., Aquino, K., Deal, R., Garbini, J., Swami, S., Tuttle, A., Xanthos, G., 2016. The influence of solar-induced thermal stresses on the mechanical weathering of rocks in humid mid-latitudes. Earth Surface Processes and Landforms 41(5), 603–614.

Alewell, C., Meusburger, K., Juretzko, G., Mabit, L., Ketterer, M.E., 2014. Suitability of $^{239+240}$Pu and ^{137}Cs as tracers for soil erosion assessment in mountain grasslands. Chemosphere 103, 274–280.

Amato, A., Aucelli, P.P.C., Cinque, A., 2003. The long-term denudation rate of in the Southern Apennine Chain: A GIS-aided estimation of the rock volumes eroded since Middle Pleistocene time. Quaternary International 101-102, 3-11.

Anderson, S.P., 2019. Breaking it down: mechanical processes in the weathering engine. Elements, 247-252.

Apollaro, C., Marini, L., Critelli, T., De Rosa, R., 2013. The standard thermodynamic properties of vermiculites and prediction of their occurrence during water–rock interaction. Applied Geochemistry 35, 264–278.

Aucelli, P.P.C., Conforti, M., Della Seta, M., Del Monte, M., D'Uva, L., Rosskopf, C.M., Vergari, F., 2016. Multi-temporal digital photogrammetric analysis for quantitative assessment of soil erosion rates in the Landola catchment of the Upper Orcia Valley (Tuscany, Italy). Land Degradation and Development 27 (4), 1075-1092.

Barnhisel, R.I., Bertsch, P.M., 1989. Chlorite and hydroxyl-interlayered vermiculite and smectite. In: Dixon, G.B., Weed, S.B. (Eds.), Minerals in soil environments, 2nd ed. Soil science Society of America, Book Series, vol. 1. Madison, Wisconsin, pp. 729–788.

Bétard, F., Caner, L., Gunnell, Y., Bourgeon, G., 2009. Illite neoformation in plagioclase during weathering: evidence from semi-arid Northeast Brazil. Geoderma 152, 53–62.

Bierman, P.R., Caffee, M., 2001. Slow rates of rock surface erosion and sediment production across the Namib Desert and escarpment, southern Africa. American Journal of Science 301, 326–358.

Biondino, D., Borrelli, L., Critelli, S., Muto, F., Apollaro, C., Coniglio, S., Tripodi, V., Perri, F., 2020. A multidisciplinary approach to investigate weathering processes affecting gneissic rocks (Calabria, southern Italy). Catena 187, 104732, 1-17.

Boelhouwers, J., Jonsson, M., 2013. Critical assessment of the 2 °C min– 1 threshold for thermal stress weathering. Geografiska Annaler: Series A, Physical Geography 95, 285–293.

Bonardi, G., Cavazza, W., Perrone, V., Rossi, S., 2001. Calabria-Peloritani Terrane and Northern Ionian Sea. In: Vai, G.B., Martini, J.P. (Eds.), Anatomy of an Orogen: the Apennines and the Adjacent Mediterranean Basins. Kluwer Academic, Norwell, MA, pp. 287–306.

Bonneau, D.A., Hutchinson, D.J., 2019. The use of terrestrial laser scanning for the characterization of a cliff-talus system in the Thompson River Valley, British Columbia, Canada. Geomorphology 327, 598–609.

Borrelli, L., Greco, R., Gullà, G., 2007. Weathering grade of rock masses as a predisposing factor to slope instabilities: Reconnaissance and control procedures. Geomorphology 87, 158-175.

Borrelli, L., Perri, F., Critelli, S., Gullà, G., 2014. Characterization of granitoid and gneissic weathering profiles of the Mucone River basin (Calabria, southern Italy). Catena 113, 325–340.

Borrelli, L., Critelli, S., Gullà, G., Muto, F., 2015. Weathering grade and geotectonics of the western-central Mucone River basin (Calabria, Italy). Journal of Maps, 11 (4), 606-624.

Borrelli, L., Coniglio, S., Critelli, S., La Barbera, A., Gullà, G., 2016. Weathering grade in granitoid rocks: The San Giovanni in Fiore area (Calabria, Italy). Journal of Maps, 12 (2), 260-275.

Borrelli, L., Ciurleo, M., Gullà, G., 2018. Shallow landslide susceptibility assessment in granitic rocks using GIS-based statistical methods: the contribution of the weathering grade map. Landslides 15 (6), 1127-1142.

Formatted: English (United Kingdom)

Formatted: English (United Kingdom)

Formatted: English (United Kingdom)

Formatted: English (United Kingdom)

Formatted: Italian (Italy)

Formatted: Italian (Italy)

900 Brodu, N., Lague, D., 2012. 3D terrestrial lidar data classification of complex natural scenes using
901 a multi-scale dimensionality criterion: Applications in geomorphology. ISPRS Journal of
902 Photogrammetry and Remote Sensing 68, 121-134.
903 Butzer, K.W., 1976. Geomorphology from the Earth. Harper and Row Publishers, New York, 463
904 pp.
905 Calero, J., Delgado, R., Delgado, G., Martín-García, J.M., 2008. Transformation of categorical field
906 soil morphological properties into numerical properties for the study of chronosequences.
907 Geoderma 145 (3–4), 278-287.
908 Caputo, T., Marino, E., Matano, F., Somma, R., Troise, C., De Natale, G., 2018. Terrestrial Laser
909 Scanning (TLS) data for the analysis of coastal tuff cliff retreat: application to Coroglio cliff,
910 Naples, Italy. Annals of Geophysics 61 (1), SE110, 1-18.
911 Chigira, M., Yokoyama, O., 2005. Weathering profile of non-welded ignimbrite and the water
912 infiltration behavior within it in relation to the generation of shallow landslides. Engineering
913 Geology 78, 187-207.
914 Cirrincione, L., Fazio, E., Fiannacca, P., Ortolano, G., Pezzino, A., Punturo, R., 2015. The
915 Calabria-Peloritani Orogen, a composite terrane in Central Mediterranean; its overall
916 architecture and geodynamic significance for a pre-Alpine scenario around the Tethyan basin.
917 Periodico di Mineralogia 84, 3B (Special Issue), 701-749.
918 Conforti, M., Buttafuoco, G., 2017. Assessing space–time variations of denudation processes and
919 related soil loss from 1955 to 2016 in southern Italy (Calabria region). Environmental Earth
920 Sciences 76, 457.
921 Cornu, S., Montagne, D., Vasconcelos, P.M., 2009. Dating constituent formation in soils to
922 determine rates of soil processes: A review. Geoderma 153, 293–303.
923 Critelli, S., Muto, F., Tripodi, V., Perri, F., 2011. Relationships between lithospheric flexure, thrust
924 tectonics and stratigraphic sequences in foreland setting: the southern Apennines foreland
925 basin system, Italy. In: Schattner, U. (Ed.), New Frontiers in Tectonic Research — at the Midst
926 of Plate Convergence. InTech, Rijeka, pp. 121–170.
927 Curry, A.M., Morris C.J., 2004. Lateglacial and Holocene talus slope development and rockwall
928 retreat on Mynydd Du, UK. Geomorphology 58, 85-106.
929 Cyr, A.J., Granger, D.E., Olivetti, V., Molin, P., 2014. Distinguishing between tectonic and lithologic
930 controls on bedrock channel longitudinal profiles using cosmogenic 10Be erosion rates and
931 channel steepness index. Geomorphology 209, 27–38.
932 Day, S.S., Gran, K.B., Belmont, P., Wawrzyniec, T., 2013a. Measuring bluff erosion part 1:
933 Terrestrial laser scanning methods for change detection and determining bluff erosion
934 processes. Earth Surface Processes and Landforms 38, 1055–1067.
935 Day, S.S., Gran, K.B., Belmont, P., Wawrzyniec, T., 2013b. Measuring bluff erosion part 2: Pairing
936 aerial photographs and terrestrial laser scanning to create a watershed scale sediment budget.
937 Earth Surface Processes and Landforms 3, 1068–1082.
938 Domènech, G., Corominas, J., Mavrouli, O., Merchel, S., Abellán, A., Pavetich, S., Rugel, G.,
939 2018. Calculation of the rockwall recession rate of a limestone cliff, affected by rockfalls, using
940 cosmogenic chlorine-36. Case study of the Montsec Range (Eastern Pyrenees, Spain).
941 Geomorphology 306, 325–335.
942 Dosseto, A., Turner, S.P., Chappell, J., 2008. The evolution of weathering profiles through time:
943 new insights from uranium-series isotopes. Earth and Planetary Science Letters 274, 359–371.
944 Dosseto, A., Menozzi, D., Kinsley, L.P.J., 2019. Age and rate of weathering determined using
945 uranium-series isotopes: Testing various approaches. Geochimica et Cosmochimica Acta 246,
946 213–233.
947 Duszyński, F., Migoń, P., Strzelecki, M.C., 2019. Escarpment retreat in sedimentary tablelands and
948 cuesta landscapes – Landforms, mechanisms and patterns. Earth-Science Reviews 196,
949 102890, 1-49.
950 Egli, M., Brandová, D., Böhlert, R. Favilli, F., Kubik, P., 2010. ^{10}Be inventories in Alpine soils and
951 their potential for dating land surfaces. Geomorphology 119, 62-73.
952 Eppes, M.C., Hancock, G.S., Chen, X., Arey, J., Dewers, T., Huettenmoser, J., Kiessling, S.,
953 Moser, F., Tannu, N., Weiserbs, B., Whitten, J., 2018. Rates of subcritical cracking and long-
954 term rock erosion. Geology 46 (11), 951–95.

Eppes, M.C., Magi, B., Hallet, B., Delmelle, E., Mackenzie-Helnwein, P., Warren, K., Swami, S., 2016. Deciphering the role of solar-induced thermal stresses in rock weathering. Geological Society of America Bulletin 128 (9-10), 1315–1338.
Eppes, M.C., Keanini, R., 2017. Mechanical weathering and rock erosion by climate-dependent subcritical cracking. Reviews of Geophysics 55, 470-508.
Fanos, A.M., Pradhan, B., 2019. A novel rockfall hazard assessment using laser scanning data and 3D modelling in GIS. Catena 172, 435–450.
Fedo, C.M., Nesbitt, H.V., Young, G.M., 1995. Unraveling the effects of potassium metasomatism in sedimentary rocks and paleosols, with implications for paleoweathering conditions and provenance. Geology 23, 921–924.
Festa, V., Langone, A., Caggianelli, A., Rottura A., 2010. Dike magmatism in the Sila Grande (Calabria, southern Italy): Evidence of Pennsylvanian–Early Permian exhumation. Geosphere 6 (6), 549-566.
Finzi, Y., Harlev, N., 2016. A regional approach for modeling cliff retreat rate: the Makhteshim Country, Israel. Geomorphology 271, 65–73.
Fischer, L., Eisenbeiss, H., Kääb, A., n Huggel, C., Haeberli, W., 2011. Monitoring topographic changes in a periglacial high-mountain face using high-resolution DTMs, Monte Rosa east face, Italian Alps. Permafrost and Periglacial Processes 22,140-152.
Galli, P., Scionti, V., Spina, V., 2007. New paleoseismic data from the Lakes and Serre faults: seismotectonic implications for Calabria (Southern Italy). Bollettino della Società Geologica Italiana 126 (2), 347-364.
Geotechnical Engineering Office – GEO, 1988. Guide to Rock and Soil Descriptions. Civil Engineering Department. The Government of the Hong Kong Special Administrative Region, Hong Kong, pp. 186.
Girardeau-Montaut, D., 2015. Cloud Compare (Version 2.9): 3D Point Cloud and Mesh Processing Software Open Source Project. EDF R&D, Telecom ParisTech http://www.danielgm.net/cc/ (Accessed 12.12.2018).
Gómez-Heras, M., Smith, B.J., Fort, R., 2006. Surface temperature differences between minerals in crystalline rocks: Implications for granular disaggregation of granites through thermal fatigue. Geomorphology 78 (3–4), 236-249.
Goodfellow, B.W., Hilley, G.E., Webb, S.M., Sklar, L.S., Moon, S., Olson, C.A., 2016. The chemical, mechanical, and hydrological evolution of weathering granitoid. Journal of Geophysical Research – Earth Surface 121, 1410–1435.
Goudie, A.S. (Ed.), 2004. Encyclopedia of Geomorphology, Routledge, New York, 1156 pp.
Granger, D.E., Riebe, C.S., 2014. Chapt. 7.12: Cosmogenic Nuclides in Weathering and Erosion. Treatise on Geochemistry (2nd edition), Vol. 7, pp. 401-436.Granger, D.E., Riebe, C.S., Kirchner, J.W., Finkel, R.C., 2001. Modulation of erosion on steep granitic slopes by boulder armoring, as revealed by cosmogenic ^{26}Al and ^{10}Be. Earth and Planetary Science Letters 186, 269–281.
Gullà, G., Matano, F., 1997. Surveys of weathering profile on gneiss cutslopes in northern Calabria, Italy. Proceedings of the International Symposium on Engineering Geology and the Environment, IAEG, Athens, Greece, 23–27 June 1997, pp. 133–138.
Gunnell, Y., Jarman, D., Braucher, R., Calvet, M., Delmas, M., Leanni, L., Bourlès, D., Arnold, M., Aumaître, G., Keddaouche, K., 2013. The granite tors of Dartmoor, Southwest England: rapid and recent emergence revealed by Late Pleistocene cosmogenic apparent exposure ages. Quaternary Science Reviews 61, 62–76.
Gutiérrez Elorza, M., Sesé Martínez, V.H., 2001.Multiple talus flatirons, variations of scarp retreat rates and the evolution of slopes in Almazán Basin (semi-arid central Spain). Geomorphology 38, 19–29.
Hartmeyer, I., Keuschnig, M., Delleske, R., Krautblatter, M., Lang, A., Schrott, L., Prasicek, G., Otto, J.-C., 2020. A 6-year LiDAR survey reveals enhanced rockwall retreat and modified rockfall magnitudes/frequencies in deglaciating cirques. Earth Surface Dynamics 8, 753–768.
Heimsath, A.M., Dietrich, W.E., Nishiizumi, K., Finkel, R.C., 1997. The soil production rate function and landscape equilibrium. Nature 388, 358-361.

1009 Heimsath, A.M., Chappell, J., Dietrich, W.E., Nishiizumi, K., Finkel, R.C., 2001. Late Quaternary
1010 erosion in southeastern Australia: a field example using cosmogenic nuclides. Quaternary
1011 International 83–85, 169–185.
1012 Heimsath, A.M., DiBiase, R.A., Whipple, K.X., 2012. Soil production limits and the transition to
1013 bedrock-dominated landscapes. Nature 5, 210-214.
1014 Hinchliffe, S., Ballantyne, C.K., 1999. Talus accumulation and rockwall retreat, Trotternish, Isle of
1015 Skye, Scotland. Scottish Geographical Journal 115, 53–70.
1016 Hinderer, M., 2012. From gullies to mountain belts: A review of sediment budgets at various
1017 scales. Sedimentary Geology 280, 21–59.
1018 Isherwood, D., Street, A., 1976. Biotite-induced grussification of Boulder Creek Granodiorite,
1019 Boulder County, Colorado: Geological Society of America Bulletin 87, 366–370.
1020 Katz, O., Mushkin, A., 2013. Characteristics of sea-cliff erosion induced by a strong winter storm in
1021 the eastern Mediterranean. Quaternary Research 80, 20–32.
1022 Kottek, M., Grieser, J., Beck, C., Rudolf, B., Rubel, F., 2006. World Map of the Köppen-Geiger
1023 climate classification updated. Meteorologische Zeitschrift 15, 259-263.
1024 Kuhn, D., Prüfer, S., 2014. Coastal cliff monitoring and analysis of mass wasting processes with
1025 the application of terrestrial laser scanning: A case study of Rügen, Germany. Geomorphology
1026 213, 153–165.
1027 Lague, D., Brodu, N., Leroux, J., 2013. Accurate 3D comparison of complex topography with
1028 terrestrial laser scanner: Application to the Rangitikei canyon (N-Z). ISPRS Journal of
1029 Photogrammetry and Remote Sensing 82, 10–26.
1030 Lair, G.J., Zehetner, F., Hrachowitz, M., Franz, N., Maringer, F.-J., Gerzabek, M.H., 2009. Dating
1031 of soil layers in a young floodplain using iron oxide crystallinity. Quaternary Geochronology 4
1032 (3), 260-266.
1033 Lamp, J.L., Marchant, D.R., Mackay, S.L., Head, J.W., 2017. Thermal stress weathering and the
1034 spalling of Antarctic rocks. Journal of Geophysical Research Earth Surface 122 (1), 3-24.
1035 Le Pera, E., Arribas, J., Critelli, S., Tortosa, A., 2001. The effects of source rocks and chemical
1036 weathering on the petrogenesis of siliciclastic sand from the Neto River (Calabria, Italy):
1037 Sedimentology 48, 357–378.
1038 Le Pera, E., Sorriso-Valvo, M., 2000. Weathering and morphogenesis in a Mediterranean climate,
1039 Calabria, Italy. Geomorphology 34, 251–270.
1040 Liotta, D., Caggianelli, A., Kruhl, J.H., Festa, V., Prosser, G., Langone, A., 2008. Multiple injections
1041 of magmas along a Hercynian mid-crustal shear zone (Sila Massif, Calabria, Italy). Journal of
1042 Structural Geology 30, 1202–1217.
1043 Martino, C., Nico, G., Schiattarella, M., 2009. Quantitative analysis of InSAR Digital Elevation
1044 Models for identification of areas with different tectonic activity in southern Italy. Earth Surface
1045 Processes and Landforms 34, 3–15.
1046 Matmon, A., Shaked, Y., Porat, N., Enzel, Y., Finkel, R., Lifton, N., Boaretto, E., Agnon, A., 2005.
1047 Landscape development in a hyperarid sandstone environment along the margins of the Dead
1048 Sea fault: Implications from dated rock falls. Earth and Planetary Science Letters 240, 803–817.
1049 Matmon, A., Mushkin, A., Enzel, Y., Grodek, T., ASTER Team, 2013. Erosion of a granite
1050 inselberg, Gross Spitzkoppe, Namib Desert. Geomorphology 201, 52–59.
1051 Martel, S.J., 2006. Effect of topographic curvature on near-surface stresses and application to
1052 sheeting joints, Geophysical Research Letters 33, L01308, 1-5.
1053 Messina, A., Barbieri, M., Compagnoni, R., De Vivo, B., Perrone, V., Russo, S., Scott, B.A., 1991.
1054 Geological and petrochemical study of the Sila Massif plutonic rocks (northern Calabria, Italy).
1055 Bollettino della Societa Geologica Italiana 110, 165–206.
1056 Messina, A., Somma, R., Macaione, E., Carbone, G., Careri, G., 2004. Peloritani continental crust
1057 composition (southern Italy): geological and petrochemical evidence. Bollettino della Società
1058 Geologica Italiana 123, 405–441.
1059 Meusburger, K., Mabit, L., Ketterer, M., Park, J. H., Sandor, T., Porto, P., Alewell, C., 2016. A
1060 multi-radionuclide approach to evaluate the suitability of $^{239+240}$Pu as soil erosion tracer. Science
1061 of the Total Environment 566, 1489–1499.
1062 Migoń, P., Vieira, G., 2014. Granite geomorphology and its geological controls, Serra da Estrela,
1063 Portugal. Geomorphology 226, 1–14.

Molin, P., Pazzaglia, F.J., Dramis, F., 2004. Geomorphic expression of active tectonics in a rapidly-deforming forearc, Sila Massif, Calabria, southern Italy. American Journal of Science 304, 559–589.
Molin, P., Fubelli, G., Dramis, F., 2012. Evidence of tectonic influence on drainage evolution in an uplifting area: the case of northern Sila (Calabria, Italy). Geografia Fisica e Dinamica Quaternaria 35, 49-60.
Mulyanto, B., Stoops, G., Van Ranst, E., 1999. Precipitation and dissolution of gibbsite during weathering of andesitic boulders in humid tropical West Java, Indonesia. Geoderma 89, 287–305.
Nadal-Romero, E., Revuelto, J., Errea, P., and López-Moreno, J. I., 2015. The application of terrestrial laser scanner and SfM photogrammetry in measuring erosion and deposition processes in two opposite slopes in a humid badlands area (central Spanish Pyrenees), SOIL 1, 561–573.
Nesbitt, H.V., Young, G.M., 1982. Early Proterozoic climates and plate motions inferred from major element chemistry of lutites. Nature 299, 715–717.
Oguchi, C.T., 2013. Weathering Rinds: Formation Processes and Weathering Rates. In: Shroder, J. (Ed.), Treatise on Geomorphology, Volume 4, Chapter 4.6, Academic Press, San Diego, pp. 98-110.
Olivetti, V., Cyr, A.J., Molin, P., Faccenna, C., Granger, D.E., 2012. Uplift history of the Sila Massif, southern Italy, deciphered from cosmogenic ^{10}Be erosion rates and river longitudinal profile analysis. Tectonics 31, 1–19, TC3007.
Pelle, T., Scarciglia, F., Di Pasquale, G., Allevato, E., Marino, D., Robustelli, G., La Russa, M.F., Pulice, I., 2013. Multidisciplinary study of Holocene archaeological soils in an upland Mediterranean site: natural versus anthropogenic environmental changes at Cecita Lake, Calabria, Italy. Quaternary International 303, 163–179.
Pérez-Peña, J.V., Azañón, J.M., Azor, A., Tuccimei, P., Della Seta, M., Soligo, M., 2009. Quaternary landscape evolution and erosion rates for an intramontane Neogene basin (Guadix-Baza basin, SE Spain). Geomorphology 106, 206–218.
Phillips, W.M., Hall, A.M., Mottram, R., Fifield, L.K., Sugden, D.E., 2006.Cosmogenic ^{10}Be and ^{26}Al exposure ages of tors and erratics, Cairngorm Mountains, Scotland: Timescales for the development of a classic landscape of selective linear glacial erosion. Geomorphology 73, 222–245.
Perri, F., 2020. Chemical weathering of crystalline rocks in contrasting climatic conditions using geochemical proxies: An overview. Palaeogeography, Palaeoclimatology, Palaeoecology 556, 109873, 1-15.
Perri, F., Scarciglia, F., Apollaro, C., Marini, L., 2015. Characterization of granitoid profiles in the Sila Massif (Calabria, southern Italy) and reconstruction of weathering processes by mineralogy, chemistry, and reaction path modeling. Journal of Soils and Sediments 15 (6), 1351–1372.
Pope, G.A., 2013. Weathering and sediment genesis. In: Shroder, J.F. (Ed.), Treatise on geomorphology 4, Weathering and soils geomorphology. Academic Press, San Diego, pp. 284–293 (chapter 17).
Raab, G., Martin, A.P., Norton, K., Christl, M., Scarciglia, F., Egli, M., 2021. Complex patterns of schist tor exposure and surface uplift, Otago (New Zealand). Geomorphology 389, 107849, 1-18.
Raab, G., Scarciglia, F., Norton, K., Dahms, D., Brandová, D., de Castro Portes, R., Christl, M., Ketterer, M.E., Ruppli, A., Egli, M., 2018. Denudation variability of the Sila Massif upland (Italy) from decades to millennia using ^{10}Be and $^{239+240}$Pu. Land Degradation & Development 29, 3736-3752.
Raab, G., Scarciglia, F., Norton, K., Dahms, D., Brandová, D., Christl, M., Egli, M., 2019. Revealing temporal and spatial denudation variations along a granitic upland relief in Italy (Sila Massif) using in-situ ^{10}Be on a variety of landscape features. Earth Surface Processes and Landforms 44, 2570–2586.
Rempel, A.W., Marshall, J.A., Roering, J.J., 2016. Modeling relative frost weathering rates at geomorphic scales. Earth and Planetary Science Letters 453, 87-95.

Riebe, C.S., Kirchner, J.W., Granger, D.E., Finkel, R.C., 2000. Erosional equilibrium and disequilibrium in the Sierra Nevada, inferred from cosmogenic ^{26}Al and ^{10}Be in alluvial sediment. Geology 28, 803–806.

Roquero, E., Silva, P.G., Goy, J.L., Zazo, C., Massana, J., 2015. Soil evolution indices in fluvial terrace chronosequences from central Spain (Tagus and Duero fluvial basins). Quaternary International 376, 101-113.

Rowe, E., Hutchinson, D.J., Kromer, R.A., 2018. An analysis of failure mechanism constraints on pre-failure rock block deformation using TLS and roto-translation methods. Landslides 15, 409–421.

Salvini, R., Francioni, M., Riccucci, S., Bonciani, F., Callegari, I., 2013. Photogrammetry and laser scanning for analyzing slope stability and rock fall runout along the Domodossola–Iselle railway, the Italian Alps. Geomorphology 185, 110–122.

Scarciglia, F., 2015. Weathering and exhumation history of the Sila Massif upland plateaus, southern Italy: a geomorphological and pedological perspective. Journal of Soils and Sediments 15 (6), 1278–1291.

Scarciglia, F., Le Pera, E., Critelli, S., 2007. The onset of the sedimentary cycle in a midlatitude upland environment: weathering, pedogenesis, and geomorphic processes on plutonic rocks (Sila Massif, Calabria). In: Arribas, J., Critelli, S., Johnsson, M.J. (Eds.), Sedimentary Provenance and Petrogenesis: Perspectives from Petrography and Geochemistry. Geological Society of America Special Paper 420. pp. 149–166.

Scarciglia, F., Pelle, T., Pulice, I., Robustelli, G., 2015. A comparison of Quaternary soil chronosequences from the Ionian and Tyrrhenian coasts of Calabria, southern Italy: rates of soil development and geomorphic dynamics. Quaternary International 376, 146–162.

Scarciglia, F., Critelli, S., Borrelli, L., Coniglio, S., Muto, F., Perri, F., 2016. Weathering profiles in granitoid rocks of the Sila Massif uplands, Calabria, southern Italy: new insights into their formation processes and rates. Sedimentary Geology 336, 46–67.

Scarciglia, F., Nicolaci, A., Del Bianco, S., Pelle, T., Soligo, M., Tuccimei, P., Marzaioli, F., Passariello, I., Iovino, F., 2020. Reforestation and soil recovery in a Mediterranean mountain environment: Insights into historical geomorphic and vegetation dynamics in the Sila Massif, Calabria, southern Italy. Catena 104707, 1-20.

Sequeira Braga, M.A., Paquet, H., Begonia, A., 2002. Weathering of granites in a temperate climate (NW Portugal): granitic saprolites and arenization. Catena 49, 41–56.

Schiattarella, M., Di Leo, P., Beneduce, P., Giano, S.I., Martino, C., 2006. Tectonically driven exhumation of a young orogen: an example from the southern Apennines, Italy. Geological Society of America Special Paper 398, 371–385.

Schiattarella, M., Giano, S.I., Gioia, D., Martino, C., Nico, G., 2013. Age and statistical properties of the summit paleosurface of southern Italy. Geografia Fisica e Dinamica Quaternaria 36 (2), 289–302.

Siewert, M.B., Krautblatter, M., Christiansen, H.H., Eckerstorfer, M., 2012. Arctic rockwall retreat rates estimated using laboratory-calibrated ERT measurements of talus cones in Longyeardalen, Svalbard. Earth Surface Processes and Landforms 37, 1542–1555.

Small, E.E., Anderson, R.S., Repka, J.L., Finkel, R., 1997. Erosion rates of alpine bedrock summit surfaces deduced from in situ ^{10}Be and ^{26}Al. Earth and Planetary Science Letters 150, 413–425.

Sorriso-Valvo, M., 1993, The geomorphology of Calabria: A sketch. Geografia Fisica e Dinamica Quaternaria 16, 75–80.

Spina, V., Galli, P., Tondi, E., Critelli, S., Cello, G., 2007. Kinematics and structural properties of an active fault zone in the Sila Massif (Northern Calabria, Italy). Bollettino della Società Geologica Italiana 126 (2), 427–438.

Sun, M., Wu, W., Ji, X., Wang, X., Qu, S., 2019. Silicate weathering rate and its controlling factors: A study from small granitic watersheds in the Jiuhua Mountains. Chemical Geology 504, 253–266.

Taboada, T., García, C., 1999a. Pseudomorphic transformation of plagioclases during the weathering of granitic rocks in Galicia (NW Spain). Catena 35, 291–302.

Taboada, T., García, C., 1999b. Smectite formation produced by weathering in a coarse granite saprolite in Galicia (NW Spain): Catena 35, 281–290.

Telling, J., Lyda, A., Hartzell, P., Glennie, C., 2017. Review of Earth science research using terrestrial laser scanning. Earth-Science Reviews 169, 35–68.
Van Dijk, J.P., Bello, M., Brancaleoni, G.P., Cantarella, G., Costa, V., Frixa, A., Golfetto, F., Merlini, S., Riva, M., Torricelli, S., Toscano, C., Zerilli, A., 2000. A regional structural model for the northern sector of the Calabrian Arc (southern Italy). Tectonophysics 324, 267–320.
Vanwalleghem, T., Stockmann, U., Minasny, B., McBratney, A.B., 2013. A quantitative model for integrating landscape evolution and soil formation. Journal of Geophysical Research – Earth Surface 118, 331–347.
Vericat, D., Smith, M.W., Brasington, J., 2014. Patterns of topographic change in sub-humid badlands determined by high resolution multi-temporal topographic surveys. Catena 120, 164–176.
Vierra, E.J., Webb, H., Girty, G.H., 2018. Unravelling the development of a spheroidally weathered diorite-gabbro, Santa Margarita Ecological Reserve, Peninsular Ranges, southern California, USA. Catena 163, 297–310.
Viles, H., 2001. Scale issues in weathering studies. Geomorphology 41, 63–72.
Viles, H., 2013. Synergistic Weathering Processes. In: Shroder, J. (Ed.), Treatise on Geomorphology, Volume 4, Chapter 4.2, Academic Press, San Diego, pp. 12-26.
von Eynatten, H., Tolosana-Delgado, R., Karius, V., Bachmann, K., Caracciolo, L., 2016. Sediment generation in humid Mediterranean setting: Grain-size and source-rock control on sediment geochemistry and mineralogy (Sila Massif, Calabria). Sedimentary Geology 336, 68-80.
Westaway, R., 1993. Quaternary uplift of Southern Italy. Journal of Geophysical Research 98, 21741–21772.
Willenbring, J.K., von Blanckenburg, F., 2010. Meteoric cosmogenic Beryllium-10 adsorbed to river sediment and soil: Applications for Earth-surface dynamics. Earth-Science Reviews 98, 105-122.